

Neural Networks for Generating Better Local Optima in Topology Optimization

Leon Herrmann^{*1}, Ole Sigmund², Viola Muning Li¹, Christian Vogl³ and Stefan Kollmannsberger⁴

¹Chair of Computational Modeling and Simulation, Technical University of Munich, School of Engineering and Design, Arcisstraße 21, Munich, 80 333, Germany

²Department of Civil and Mechanical Engineering, Technical University of Denmark. Koppels Allé, B.404, 2800 Kgs. Lyngby, Denmark

³BMW Group, Knorrstraße 147, 80937 München

⁴Chair of Data Science in Engineering, Bauhaus-Universität Weimar, Coudraystraße 13 b, 99423, Weimar, Germany

Abstract

Neural networks have recently been employed as material discretizations within adjoint optimization frameworks for inverse problems and topology optimization. While advantageous regularization effects and better optima have been found for some inverse problems, the benefit for topology optimization has been limited — where the focus of investigations has been the compliance problem. We demonstrate how neural network material discretizations can, under certain conditions, find better local optima in more challenging optimization problems, where we here specifically consider acoustic topology optimization. The chances of identifying a better optimum can significantly be improved by running multiple partial optimizations with different neural network initializations. Furthermore, we show that the neural network material discretization’s advantage comes from the interplay with the Adam optimizer and emphasize its current limitations when competing with constrained and higher-order optimization techniques. At the moment, this discretization has only been shown to be beneficial for unconstrained first-order optimization.

Keywords: topology optimization, acoustics, transfer learning, deep learning, neural networks

1. Introduction

1.1. Motivation

Although neural networks (NNs) [1] are prevalent in both topology optimization [2] and the broader field of computational mechanics [3], very few if any robust, yet efficient applications exist that outperform classical methods, as discussed in [2, 3].

In topology optimization and inverse problems, the most popular approach is learning a direct mapping between the problem setup or measurements and the quantity of interest. Examples in topology optimization include [4–7] (with extensions using specialized loss functions [8, 9], generative NN architectures [10–13], moving morphable components [14, 15], transfer learning [16], and principal components analysis [17]). In inverse problems — in which governing equations or their coefficients are identified from measurements — notable works consist of [18–21]. For various forward problems — where governing equations are solved given a set of coefficients — examples are [22–24] for fluid mechanics, [25, 26] for solid mechanics, and [27] for heat transfer — where neural operators [28–30] is one of the most recent trends. The most promising situation are inverse

^{*}leon.herrmann@tum.de, Corresponding author

problems, as data generation is not as expensive as for topology optimization, where each data point requires a full optimization instead of a single forward solve. Solving forward problems with NNs is less attractive due to competition from efficient forward solvers. However, even for inverse problems, the amount of required data is currently unviable, as, for example, seen in [31] requiring 53 007 data points for a two-dimensional inverse design problem. Exceptions are possible when the problem is reducible, as demonstrated in combination with model order reduction techniques in [32–37].

However, even when the data requirements are neglected, reliability and accuracy of purely data-driven approaches are a major issue, as pointed out in [2, 3]. Unless no accurate and efficient alternative exists or accuracy is not required¹, NNs have limited potential in replacing the entire simulation or optimization chain. However, as argued in [3], NNs might be beneficial in replacing part of the simulation or optimization chain.

1.2. Neural Network Ansatz for Optimization Problems

One such promising current trend is the discretization of the spatial material distribution for inverse problems [45–50] and topology optimization [51–57]. Specifically an NN is used to represent the design variables, thus reparametrizing design variables as NN weights. Although the variables representing the material are the same, the number of adjustable parameters can be increased. The potential of this overparametrized discretization is three-fold. Firstly, NNs introduce an implicit regularization, potentially resulting in smoother designs than with classical approaches [45, 46, 49]. Secondly, an overparametrization may be less prone to get stuck in local optima as the chances of all gradient components becoming zero simultaneously decrease. This has, however, yet to be proven. Lastly, prior information can be introduced within the NN. For example, in full waveform inversion, mappings between previous measurements and material distributions are learned through a pretraining and exploited in a subsequent full waveform inversion optimization, yielding an accelerated convergence [58–60]. This relies on the concept of transfer learning [61–63]. However, in the context of topology optimization, the advantages of an NN material discretization have been limited [54, 57]. One reason for this lack of advantage is that the focus has been on the compliance problem [64, 65], which is not a challenging optimization problem — in which ending in premature local optima is not a critical issue and can, in turn, not be improved by an NN parametrization. To this end, we investigate a more challenging optimization problem, *acoustic topology optimization*² [69–74], which is prone to get stuck in extremely diverse local optima [75]. The research question under investigation is whether discretizing the density with an NN can benefit topology optimization.

This work will refer to the classical approach, where each design variable is optimized directly, as the *linear ansatz*. When an NN predicts the design variables and the NN parameters, in turn, become the actual tunable parameters, we refer to it as the *NN ansatz*.

2. Acoustic Topology Optimization

Throughout this treatise, we consider an example from [75], illustrated in Figure 1. Given a harmonic point source s , at (x_f, y_f) excited at frequency f , a solid material (aluminum) is to be distributed in the ceiling of the domain Ω_c with height h_c . The material is to be distributed such that the sound pressure level L_p in the area Ω_s a rectangular domain of size $a_s \times b_s$ at (x_s, y_s) is minimal. The sound pressure level $L_p = 10 \log_{10}(|p|^2/p_0^2)$ depends on the wave pressures p , which are governed by the acoustic wave equation in the rectangular domain Ω of dimensions $a \times b$ filled

¹An excellent application of NNs in computational mechanics is material modeling, where many constitutive laws are based on empirical fits, which require extensive tuning by the practitioner. NNs being excellent interpolants have therefore shown benefits [38–43], see [44] for a recent review.

²with a direct connection to topology optimization for photonics, see for example [66–68]

by air with a reference pressure $p_0 = 2 \cdot 10^{-6}$ Pa [76].

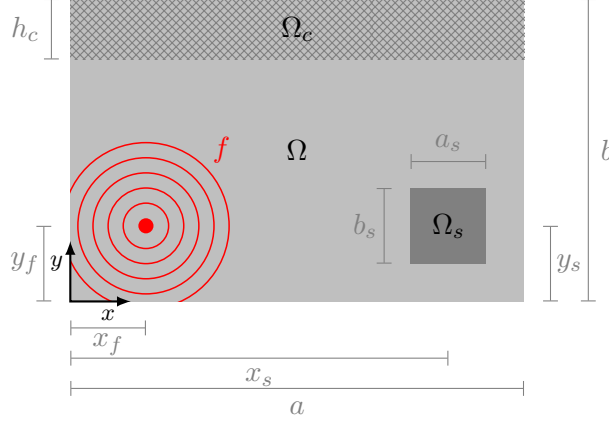


Figure 1: Topology optimization of a ceiling Ω_c of height h_c in order to suppress the sound pressure in the domain Ω_s from a harmonic source s at x_f, y_f with frequency f . The suppressed domain is rectangular with dimensions a_s, b_s and centered at x_s, y_s . The domain Ω with dimensions $a \times b$, including Ω_c and Ω_s , is governed by the acoustic wave equation.

An exemplary optimized design is depicted in Figure 2, where at a frequency of $f = 69.43$ Hz, a sound pressure level of $L_p = 110.0$ dB in the domain Ω_s is reduced to $L_p = 61.3$ dB through an optimized ceiling. The dimensions of the problem are summarized in Table 1 and will be used throughout the upcoming investigations unless stated otherwise.

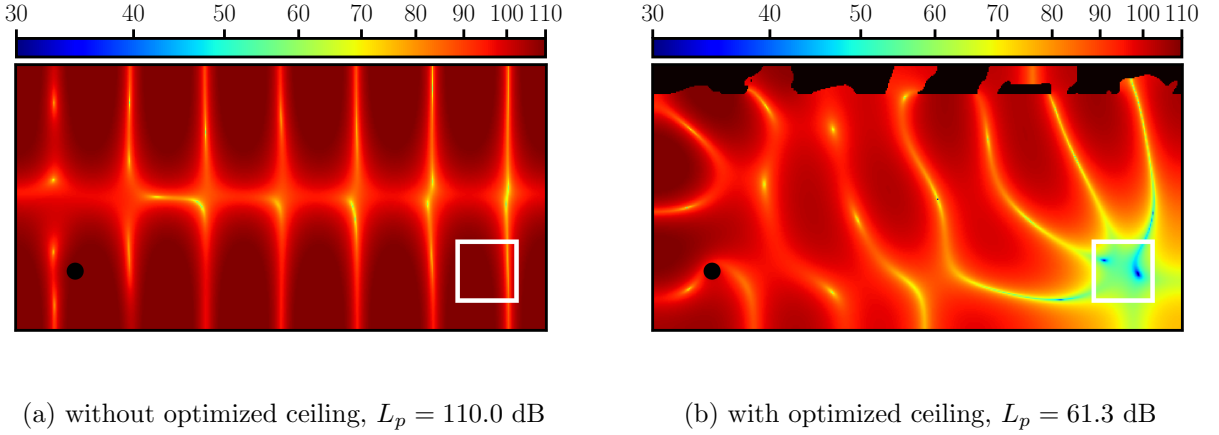


Figure 2: Sound pressure level distribution in dB at $f = 69.43$ Hz without and with an optimized ceiling

Table 1: Dimensions of the problem setup illustrated in Figure 1 and simulated in Figure 2. Dimensions are provided in meters.

a	b	h_c	x_f	y_f	x_s	y_s	a_s	b_s
18	9	1	2	2	16	2	2	2

2.1. Physical Model

The wave pressure field p is governed by the acoustic wave equation consisting of the mass density ρ , the bulk modulus κ , and a source term s . Specifically, we consider a normalized acoustic wave

equation [75] with homogeneous Neumann boundary conditions, i.e., reflecting boundary conditions and mass-proportional damping with coefficient $\eta_d = 0.01 \text{ s}^{-1}$.

$$\nabla \cdot (\tilde{\rho}^{-1} \nabla p) - \eta_d \tilde{\kappa}^{-1} \frac{\partial p}{\partial t} - \tilde{\kappa}^{-1} \frac{\partial^2 p}{\partial t^2} = s \quad (1)$$

The normalized inverse mass density $\tilde{\rho}^{-1}$ and bulk modulus $\tilde{\kappa}^{-1}$ are interpolated by the indicator ζ and the corresponding material parameters of air $\rho_1 = 1.204 \text{ kg/m}^3$, $\kappa_1 = 1.419 \cdot 10^5 \text{ N/m}^2$, and the solid material (aluminum) $\rho_2 = 2643 \text{ kg/m}^3$, $\kappa_2 = 6.87 \cdot 10^{10} \text{ N/m}^2$ [75].

$$\tilde{\rho}^{-1}(\zeta) = 1 + \zeta \left(\frac{\rho_1}{\rho_2} - 1 \right) \quad (2)$$

$$\tilde{\kappa}^{-1}(\zeta) = 1 + \zeta \left(\frac{\kappa_1}{\kappa_2} - 1 \right) \quad (3)$$

Thus, air with an indicator of $\zeta = 0$, yields $\tilde{\rho}^{-1}(0) = 1$, $\tilde{\kappa}^{-1}(0) = 1$, while the solid with an indicator of $\zeta = 1$, yields $\tilde{\rho}^{-1}(1) = \rho_1/\rho_2$, $\tilde{\kappa}^{-1}(1) = \kappa_1/\kappa_2$.

Assuming a periodic excitation $s = \hat{s}e^{-i\tilde{\omega}t}$ with the normalized angular frequency $\tilde{\omega} = \omega/\sqrt{\kappa_1/\rho_1}$, Equation (1) may be simplified to the Helmholtz equation. The transformation is carried out by assuming a solution of the form $p = \hat{p}e^{-i\tilde{\omega}t}$.

$$\nabla \cdot (\tilde{\rho}^{-1} \nabla \hat{p}) + i\tilde{\omega}\eta_d\tilde{\kappa}^{-1}\hat{p} + \tilde{\omega}^2\tilde{\kappa}^{-1}\hat{p} = \hat{s} \quad (4)$$

In the sequel, a fixed amplitude of $\hat{s} = 10 \text{ Pa/m}^2$ is chosen.

2.2. Discretization

A finite element discretization of the Helmholtz equation from Equation (4) yields the system

$$\mathbf{S}\hat{\mathbf{p}} = \mathbf{f}, \quad (5)$$

with the solution vector $\hat{\mathbf{p}}$, the source vector \mathbf{f} , and the system matrix

$$\mathbf{S} = \mathbf{K} - i\tilde{\omega}\eta_d\mathbf{M} - \tilde{\omega}^2\mathbf{M} = \mathbf{K} - (i\tilde{\omega}\eta_d + \tilde{\omega}^2)\mathbf{M} \quad (6)$$

consisting of stiffness \mathbf{K} and mass matrix \mathbf{M} . We employ high-order integrated Legendre polynomials $\Phi_i(\boldsymbol{\xi})$ [77, 78] with degree q as finite element ansatz for the scalar solution field $\hat{p}(\boldsymbol{\xi})$ within an individual element e .

$$\hat{p}_e(\boldsymbol{\xi}) = \sum_{i=1}^{(q+1)^2} \Phi_i(\boldsymbol{\xi}) \hat{p}_i \quad (7)$$

The indicator ζ and thereby the normalized inverse mass density $\tilde{\rho}^{-1}$ and bulk modulus $\tilde{\kappa}^{-1}$ are discretized with n_v subvoxels per dimension within each element, as in the multi-resolution finite cell method [79, 78]. Together with the voxel discretization of the indicator $\zeta(\boldsymbol{\xi})$ — yielding the normalized inverse mass density and bulk modulus voxel values $\tilde{\rho}_v^{-1}$, $\tilde{\kappa}_v^{-1}$, the local stiffness matrix \mathbf{k}_e and local mass matrix \mathbf{m}_e can be constructed as

$$\mathbf{k}_e = \sum_v \tilde{\rho}_v^{-1} \int_{\Omega_v} \mathbf{k}(\boldsymbol{\xi}) d\Omega_v = \sum_v \tilde{\rho}_v^{-1} \mathbf{k}_v, \quad (8)$$

$$\mathbf{m}_e = \sum_v \tilde{\kappa}_v^{-1} \int_{\Omega_v} \mathbf{m}(\boldsymbol{\xi}) d\Omega_v = \sum_v \tilde{\kappa}_v^{-1} \mathbf{m}_v. \quad (9)$$

This is achieved most efficiently through preintegration [80], where the stiffness $\mathbf{k}(\boldsymbol{\xi})$ and mass matrix integrands $\mathbf{m}(\boldsymbol{\xi})$ are integrated separately on each subvoxel domain Ω_v , yielding the stiffness \mathbf{k}_v and mass matrix contribution \mathbf{m}_v of each subvoxel v . Thus leading to only a single local integration valid for all equally sized elements and all subsequent optimization iterations.

In the subsequent analyses, we will always consider a material grid discretized by 432×216 voxels. The number of elements (i.e., finite cells) thus depends on the number of subvoxels n_v per element.

2.3. Optimization

With the governing physics and a corresponding discretization, the cost function C can be formulated. As introduced in Figure 1, the aim is to minimize the sound pressure level L_p in the domain Ω_s . To this end, the wave pressure is integrated in Ω_s and normalized by the area of Ω_s , yielding

$$C = \frac{1}{\int_{\Omega_s} d\Omega_s} \int_{\Omega_s} |\hat{p}|^2 d\Omega_s. \quad (10)$$

No additional constraints are enforced on the optimization. For all cases, the optimization is performed with the first-order optimizer Adam [81] — with only the learning rate α as a tuned hyperparameter. Adam is for the unconstrained acoustic topology optimization problem assessed to be superior over simple steepest descent for both the linear and NN ansatz, as similarly seen in the context of full waveform inversion [49]. Each gradient-based update is referred to as an epoch within this text, thus adopting the deep learning terminology [1].

Furthermore, the high-order multi-resolution discretization poses an additional challenge within the optimization, as previously explored for the compliance problem in [82]. In the compliance problem, optimized topologies with too low polynomial degrees q given a number of subvoxels n_v suffer from spurious artifacts, rendering the design's discretization dependent and thereby useless. By contrast, artifacts are limited in acoustic topology optimization, as explored in Appendix A. Nevertheless, errors occur, which can often be resolved by a few iterations of a second subsequent optimization with an increased polynomial degree q , i.e., acting as a correction of the obtained design. This scheme and its advantage in computational speed are explained in detail in Appendix A. This work performs the optimization with $q = 2$, $n_v = 4$ for 280 epochs, followed by $q = 4$, $n_v = 4$ until the cost function is at maximum 1.5 larger than after the initial optimization³. The second optimization is capped by 100 epochs. The final design is evaluated with $q = 2$, $n_v = 1$.

Additional tools used for the optimization are a polynomial learning rate scheduler — reducing the learning rate following the rule $(0.2 \cdot \text{epoch} + 1)^{-0.5}$ — and gradient clipping [83, 84]. Both are only employed when using NNs, as the linear ansatz does not benefit from them.

2.4. Sensitivity Analysis

In order to perform the gradient-based optimization, the gradients have to be computed, which can be achieved with an adjoint sensitivity approach, see [67] for a short, but complete derivation of the adjoint sensitivity approach with the Helmholtz equation. As outlined for acoustic topology optimization [75, 85] or more generally [86], first the adjoint equation is considered

$$\mathbf{S}^\top \hat{\mathbf{p}}^\dagger = - \left(\frac{\partial C}{\partial \hat{\mathbf{p}}_R} - i \frac{\partial C}{\partial \hat{\mathbf{p}}_I} \right)^\top, \quad (11)$$

where $\hat{\mathbf{p}}_R$ and $\hat{\mathbf{p}}_I$ are correspondingly the real and imaginary part of $\hat{\mathbf{p}}$ and $\hat{\mathbf{p}}^\dagger$ is the corresponding adjoint solution. The k^{th} entry of the right-hand side of Equation (11) is given by

$$\left(\frac{\partial C}{\partial \hat{\mathbf{p}}_R} - i \frac{\partial C}{\partial \hat{\mathbf{p}}_I} \right)_k = \frac{1}{\int_{\Omega_s} d\Omega_s} \int_{\Omega_s} 2(\hat{\mathbf{p}}_R - i\hat{\mathbf{p}}_I)_k N_k d\Omega_s. \quad (12)$$

By solving Equation (11) with the same discretization as described in Section 2.2, the adjoint solution $\hat{\mathbf{p}}^\dagger$ is obtained. With the adjoint solution, the sensitivity of the cost function C with respect to the indicator voxel values ζ_v can be computed as

$$\frac{dC}{d\zeta_v} = \frac{\partial C}{\partial \zeta_v} + \Re \left(\hat{\mathbf{p}}^\dagger \frac{\partial \mathbf{S}}{\partial \zeta_v} \hat{\mathbf{p}} \right) = \Re \left(\hat{\mathbf{p}}^\dagger \frac{\partial \mathbf{S}}{\partial \zeta_v} \hat{\mathbf{p}} \right), \quad (13)$$

³This criterion was determined empirically and can surely be improved. The intent is to prevent excessive iterations without improvement. The attained cost function values of the first optimization cannot always be reached by the second optimization. To this end, the cost function threshold is increased by a percentage, which in this work is 50%.

as described in [75, 85], where \Re extracts the real part. Equation (13) requires the system matrix sensitivity with respect to the indicator voxel values $\partial \mathbf{S} / \partial \zeta_v$, which can be computed with the stiffness matrix derivative with respect to the normalized inverse mass density $\partial \mathbf{K} / \partial \tilde{\rho}_v^{-1} = \mathbf{k}_v$, and the mass matrix derivative with respect to the normalized inverse bulk modulus $\partial \mathbf{M} / \partial \tilde{\kappa}_v^{-1} = \mathbf{m}_v$. This yields⁴

$$\frac{\partial \mathbf{S}}{\partial \zeta_v} = \frac{\partial \mathbf{K}}{\partial \tilde{\rho}_v^{-1}} \frac{\partial \tilde{\rho}_v^{-1}}{\partial \zeta_v} - (i\tilde{\omega}\eta_d + \tilde{\omega}) \frac{\partial \mathbf{M}}{\partial \tilde{\kappa}_v^{-1}} \frac{\partial \tilde{\kappa}_v^{-1}}{\partial \zeta_v}. \quad (14)$$

Inserting Equation (14) into Equation (13) results in the final expression of the cost function gradient with respect to the indicator voxel values.

$$\frac{dC}{d\zeta_v} = \Re \left(\hat{\mathbf{p}}^\dagger \left[\left(\frac{\rho_1}{\rho_2} - 1 \right) \mathbf{k}_v - (i\tilde{\omega}\eta_d + \tilde{\omega}^2) \left(\frac{\kappa_1}{\kappa_2} - 1 \right) \mathbf{m}_v \right] \hat{\mathbf{p}} \right) \quad (15)$$

2.5. Filtering and Projection

In order to avoid mesh-dependent solutions with too small and, thereby, unmanufacturable features, filtering is employed [87]. Specifically, a density filter with linear decay [88, 89] is employed⁵. The filtered indicators are given as

$$\tilde{\zeta}_v = \frac{\sum_{k \in N_v} w(\mathbf{x}_v - \mathbf{x}_k) \zeta_k}{\sum_{k \in N_v} w(\mathbf{x}_e - \mathbf{x}_k)}, \quad (16)$$

where N_v is the neighborhood of voxel v , i.e., $N_v = \{k \mid \|\mathbf{x}_k - \mathbf{x}_v\| < r_f\}$. The linear decay is enforced through the weighting function $w(\mathbf{x})$ with the filter radius r_f .

$$w(\mathbf{x}) = \begin{cases} r_f - \|\mathbf{x}\| & \text{if } \|\mathbf{x}\| \leq r_f \\ 0 & \text{else} \end{cases} \quad (17)$$

A filter radius of two voxels is employed, i.e., $r_f = 2 \cdot b/216 \approx 0.083$ m. As the filtering smears the designs and sharp designs are sought-after, a subsequent projection ensures a near 0/1- design [92–94]. To this end, a smooth approximation of the Heaviside function $H(\tilde{\zeta})$ — allowing differentiation — is employed [93], yielding projected indicator values $\tilde{\tilde{\zeta}}$ after thresholding $\tilde{\zeta}$.

$$\tilde{\tilde{\zeta}} = H(\tilde{\zeta}) = \frac{\tanh(\beta\eta) + \tanh(\beta(\tilde{\zeta} - \eta))}{\tanh(\beta\eta) + \tanh(\beta(1 - \eta))} \quad (18)$$

Here η shifts the thresholding, while β controls the sharpness. To allow a proper gradient flow from the projected indicator values $\tilde{\tilde{\zeta}}$ to the indicator values ζ , β is initially kept small and gradually increased [92, 93, 85]. Specifically, we initialize $\beta = 1$, and increase it by 2% per epoch and limit it to $\beta_{\max} = 75$ during the first optimization at $q = 2, n_v = 4$ and to $\beta_{\max} = 150$ for the second optimization at $q = 4, n_v = 4$. The threshold is set to $\eta = 1/2$.

The mass density and bulk modulus parametrization from Equations (2) and (3) thus rely on the filtered and projected indicator $\tilde{\tilde{\zeta}}$, which in turn is also considered during the sensitivity computation with Equation (15). As, the framework is implemented in PyTorch [95], the sensitivity $\partial \tilde{\tilde{\zeta}} / \partial \zeta$ can be obtained through automatic differentiation [96]. The computational cost of this operation is negligible.

3. Neural Network Ansatz

Before introducing the NN ansatz for acoustic topology optimization (Section 3.2), the motivation for using an NN ansatz is clarified on simple optimization benchmark problems (Section 3.1).

⁴Note that the sensitivity computation becomes more involved if static condensation is performed on the internal modes of the higher-order shape functions, as seen in [82].

⁵Note that acoustic topology optimization does not typically yield robust designs [85]. This can be ensured with approaches discussed in [90, 91, 85]. This is, however, neglected in this work.

3.1. Motivation for a Neural Network Ansatz

Consider the two-dimensional Rosenbrock function

$$f(x, y) = (1 - x)^2 + 100(y - x^2)^2 \quad (19)$$

with x and y as design variables. The function’s minimum is at $x = 1, y = 1$. Given an initial guess (x_0, y_0) , the design variables can be updated via gradient descent schemes to decrease f . For this, first-order optimization methods rely on the gradients $\frac{\partial f}{\partial x}$ and $\frac{\partial f}{\partial y}$.

An NN parametrization, i.e., the NN ansatz, can be introduced to represent x and y . To be more precise, an NN $a(\mathbf{z}; \boldsymbol{\Theta})$ parametrized by the NN weights $\boldsymbol{\Theta}$ predicts \hat{x} and \hat{y} from an input \mathbf{z} , where the hat symbol indicates an NN prediction.

$$\begin{bmatrix} \hat{x} \\ \hat{y} \end{bmatrix} = a(\mathbf{z}; \boldsymbol{\Theta}) \quad (20)$$

Instead of updating \hat{x} and \hat{y} directly during an optimization, the NN weights $\boldsymbol{\Theta}$ are updated utilizing the gradients $\frac{\partial f}{\partial \boldsymbol{\Theta}} = \frac{\partial f}{\partial x} \cdot \frac{\partial \hat{x}}{\partial \boldsymbol{\Theta}} + \frac{\partial f}{\partial y} \cdot \frac{\partial \hat{y}}{\partial \boldsymbol{\Theta}}$ obtained with the chain rule. This parametrization allows for the increase of the number of tunable parameters, i.e., an overparametrization. This can reduce the chances of getting stuck in a local optimum, as more gradients need to be zero than when directly optimizing x, y .

We demonstrate the potential of the NN ansatz through a comparison with the linear ansatz, i.e., treating x, y directly as design variables on the benchmark problem from Equation (19). To this end, a fully connected NN predicts \hat{x}, \hat{y} from 10 random inputs \mathbf{z} sampled from a uniform distribution in the range $[-1, 1]$. One hidden layer composed of 50 neurons is selected, determined by tuning the architecture. This yields 625 instead of two design variables. From an initial guess⁶ $x_0 = 3, y_0 = 3$ the two approaches are compared, where different NN instances are averaged — possible due to different NN weight initializations. To guarantee the same start value, the first NN output is shifted such that $\hat{x}_0 = 3, \hat{y}_0 = 3$. In both cases, the first-order optimizer Adam [81] is employed for 300 epochs, similar to the works utilizing NN material discretizations [45–57]. The corresponding learning rate α is tuned through a grid search, which only performs 20 epochs to assess the quality of an optimization.

Figure 3a compares the optimization paths along the Rosenbrock landscape, in which the NN ansatz is indicated in gray and the linear ansatz in black. For this NN instance, an advantage is apparent. However, when considering 20 NN instances obtained with different NN weight initializations, the NN is not always superior, as seen in Figure 3b. The average performance over the 20 instances is only slightly improved, although many NN instances are significantly better. This point is crucial because it demonstrates that better solutions can often be found using an indirect design variable parametrization rather than optimizing the design variables directly.

Changing the optimizer reduces the benefit. Steepest descent does not exhibit a clear advantage, as shown in Figure 4. Also, using second-order optimizers diminishes the differences, which was tested with L-BFGS [97]. A further disadvantage of only working indirectly with the true quantities of interest, i.e., x, y , arises when enforcing constraints. Popular constrained optimizers in topology optimization, such as the optimality criterion methods (see, e.g., [98]), the method of moving asymptotes [99], or the globally convergent method of moving asymptotes [100], do not provide an update direction of the design variables but an exact update of them. Currently, only directions can be transferred to the NN weights $\boldsymbol{\Theta}$. Projecting updated design variables x, y to the NN weights would require an additional non-linear optimization due to the non-linear nature of the NN. Thus, the potential advantage of an NN ansatz reduces for constrained optimization. For the compliance problem, this challenge has been tackled by enforcing the constraints via penalty terms [54–57].

⁶Different initial guesses were tested with similar outcomes.

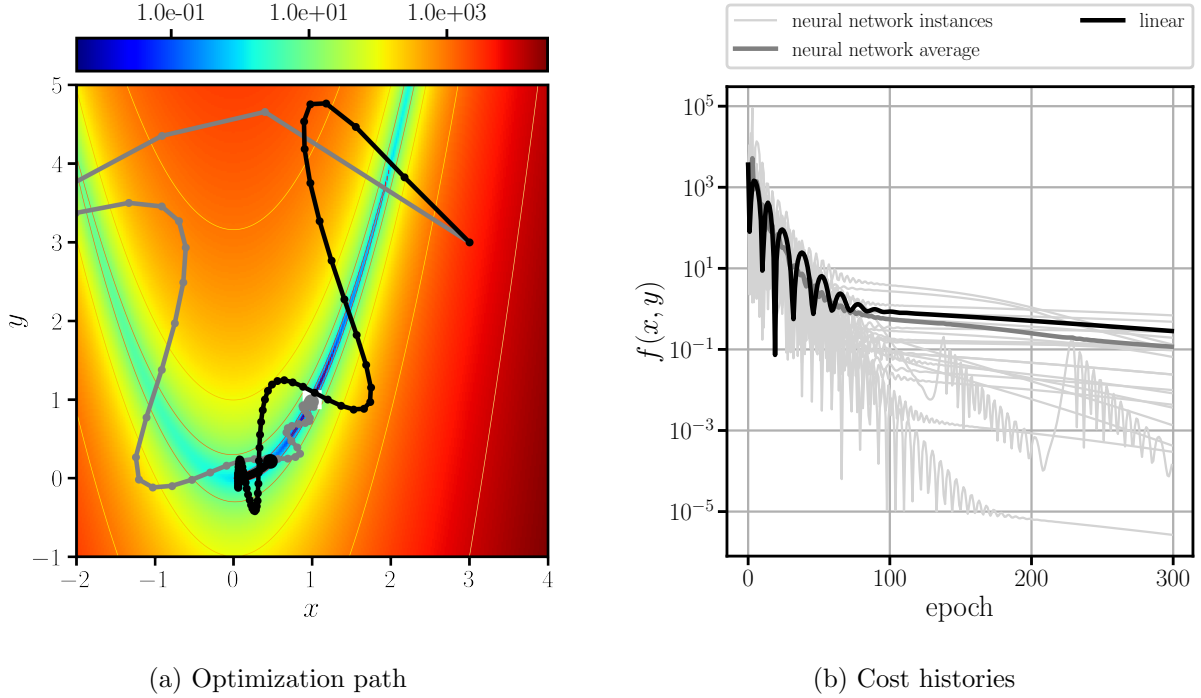


Figure 3: Rosenbrock function optimized with NN ansatz and directly on the coordinates (linear ansatz) using **Adam**

Another limitation is that the NN ansatz’s benefit is highly problem-dependent. To illustrate this, we consider three additional optimization benchmarks, the Rastrigrin, Ackley, and Lévi functions (see Appendix B for details). The optimization’s success is most sensitive to the choice of initial guess. In order to gain a statistical understanding of the method’s benefit, 4 000 optimizations with different initial guesses are performed for each of the benchmarks. The outcome is quantified by considering the percentage of the NN ansatz being superior over the linear ansatz for a given problem. The results are summarized in Table 2 for five different NN architectures. Only the number of hidden neurons is varied from 25 to 400 neurons, yielding 327 (for 25 neurons), 652 (for 50 neurons), 1 302 (for 100 neurons), 2 602 (for 200 neurons), and 5 202 (for 400 neurons) trainable parameters. The best performances are indicated with gray highlights in Table 2 and are between 50 and 100 neurons.

Table 2: Percentage of NN ansatz successfully outperforming the linear ansatz — averaged over 4 000 initial guesses with a single NN initialization and optimized learning rates α over 10 tuning epochs. The choice of initial guess is much more sensitive than the NN initialization.

	25 neurons	50 neurons	100 neurons	200 neurons	400 neurons
Rosenbrock	74.8%	77.5%	79.5%	78.2%	70.9%
Rastrigrin	53.2%	52.0%	56.6%	52.7%	47.7%
Ackley	41.3%	43.4%	44.0%	34.0%	26.8%
Lévi	48.5%	49.1%	47.9%	42.6%	37.1%

The exact reason for the deterioration of the NN ansatz success observed in Table 2 for the Rastrigrin, Ackley, and Lévi function is unclear. However, the question arises of whether an improved, problem-specific NN weight initialization can improve performance. Currently, a generic He initialization [101] is employed, whose direct aim is to ensure a good gradient flow through the NN. Transfer learning [61–63] can be seen as a problem-specific initialization, as employed in many computer vision tasks [102, 103], which are pretrained on state-of-the-art NNs such as ImageNet [104]. However, transfer learning has also successfully been applied to full waveform inversion [58–60]. In

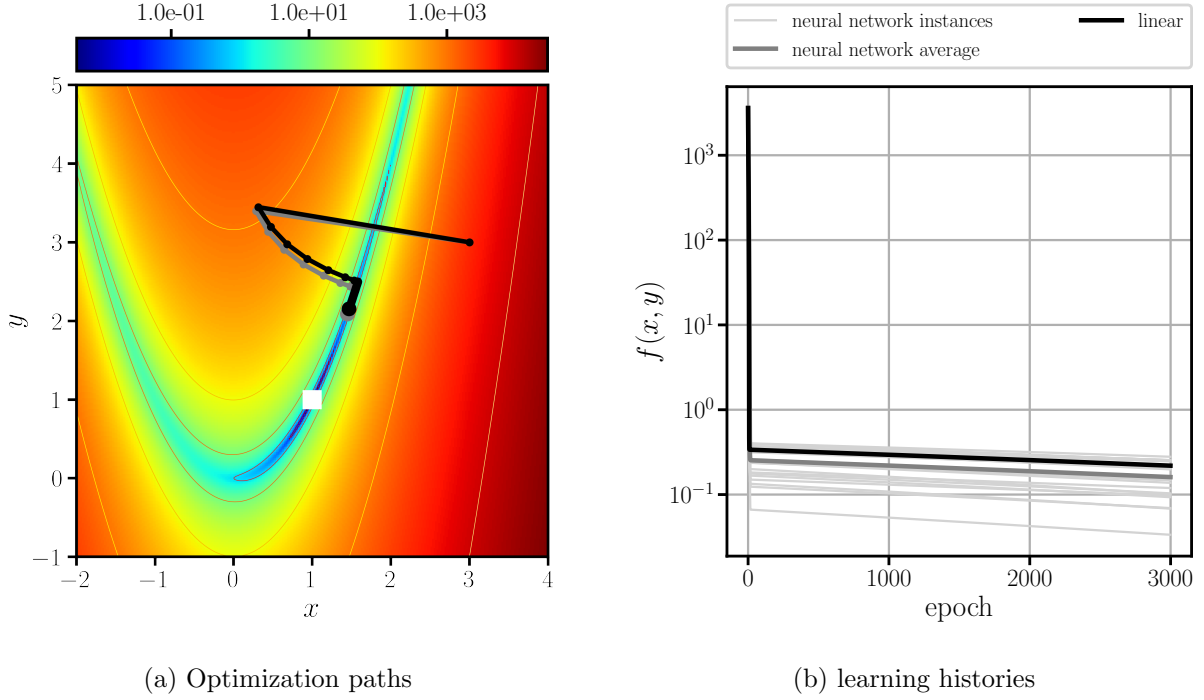


Figure 4: Rosenbrock function optimized with NN ansatz and directly on the coordinates (linear ansatz) using **steepest descent**

transfer learning, before applying the NN to a problem, it is pretrained on similar problems, thus improving convergence. As this task is highly problem-dependent, the effect of transfer learning will be studied on the acoustic topology optimization problem in the following sections.

3.2. Neural Network Ansatz for Acoustic Topology Optimization

Acoustic topology optimization will be performed on the setup described in Figure 1 with the dimensions from Table 1. The optimization is performed for distinct individual frequencies. Similarly to [75, 85], resonance frequencies are considered, where eight frequencies: 21.33 Hz, 34.39 Hz, 57.22 Hz, 69.43 Hz, 76.30 Hz, 95.37 Hz, 141.78 Hz, and 166.56 Hz were selected. The frequencies were determined as described in Appendix C. As an NN architecture, we employ a U-net with 148 806 trainable parameters (see Appendix D for details). To put this number into context, the number of design variables, i.e., voxels in the ceiling Ω_c , is $432 \times 24 = 10\,368$.

Before proceeding, the motivation of acoustic topology optimization to investigate the possibilities of an NN ansatz is clarified (Section 3.2.1) — namely, the potential of NNs to identify better designs than classically obtainable. This is followed by highlighting how the NN struggles with filtering and projection (Section 3.2.2) and how this can be overcome by transfer learning (Section 3.2.3).

3.2.1. Acoustic Topology Optimization and Neural Networks

Using NNs in acoustic topology optimization is a favorable combination mainly for two reasons. Firstly, an unconstrained optimization problem can be considered (Equation (10)) — and secondly, the optimized topologies are highly sensitive to the initial guess. Thus, different optimization runs yield very different local optima, i.e., different final designs, which can potentially be improved through smart initial guesses by the NN in order to consistently reach good local optima.

This sensitivity to the initial guess is illustrated in Figure 5, where the final design exhibits a completely different performance when changing the initial indicator guess from $\zeta = 0$ to $\zeta = 1$, as

seen for $f = 69.43$ Hz and $f = 206.31$ Hz.

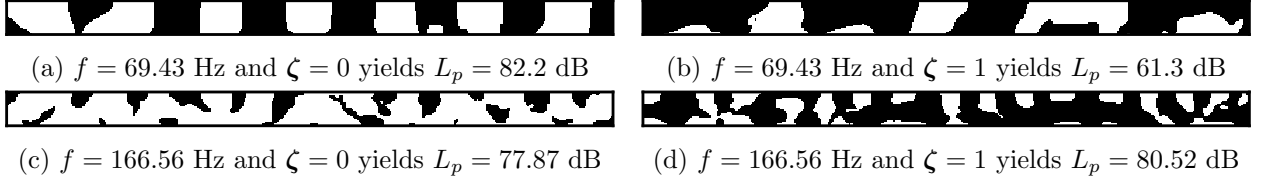


Figure 5: Optimized structure after 300 epochs (280 with $q = 2, n_v = 4$ and 20 with $q = 4, n_v = 4$) with the corresponding sound pressure level L_p in the to-be-suppressed area

3.2.2. Bypassing of Filtering and Projection

However, simply exchanging the linear ansatz with the NN ansatz in the described topology optimization framework (Section 2) yields unsatisfactory results. Figure 6 compares an optimization between the two approaches for $f = 69.43$ Hz. For simplicity, the optimization is conducted only with $q = 2, n_v = 4$, i.e., without the second optimization, acting as correction, described in Appendix A. Manufacturing restrictions require filtering and projection as described in Section 2.5. However, projecting the final design with the NN ansatz, seen in Figure 6h, yields a design that is not sharp and does not obey the filtering length scale r_f . The problem is that the filtering and projection are intended to be applied to unfiltered designs already spanning the full $[0, 1]$ range and resembling the final design, as in Figures 6c, 6e and 6g. This is not the case for the NN ansatz in Figures 6d, 6f and 6h. The cause is linked to the initialization, which consists of random noise centered around 0.5 (see Figure 6b). However, shifting the centering closer to 0 or 1 does not help. The linear ansatz does not suffer from this phenomenon independent of its initialization.

The positive side is that the NN reaches a slightly better optimum, i.e., $L_p^{\text{before}} = 59.88$ dB, compared to $L_p^{\text{before}} = 60.22$ dB with the linear ansatz. However, this phenomenon of bypassing the filtering and projection diminishes any advantage gained after thresholding the final design to the discrete 0/1 space. The design using the NN ansatz goes from $L_p^{\text{before}} = 59.88$ dB to $L_p^{\text{after}} = 70.09$ dB after thresholding, while with the linear ansatz, the thresholded design results in $L_p^{\text{after}} = 60.33$ dB. To overcome this problem, the NN initialization has to be improved, which will be achieved through transfer learning.

3.2.3. Transfer learning

To overcome the aforementioned filtering and projection bypassing problem (Section 3.2.2) and still exploit the potential identification of better local optima with an NN ansatz (Section 3.1), restarting and transfer learning are introduced. The main goal is to change the initial guess from Figure 6b to a material distribution resembling Figure 6c or Figure 6d. To this end, two schemes are proposed:

- a restarting scheme,
- transfer learning.

In the restarting scheme, an optimization with the linear ansatz is performed, followed by an optimization with an NN ansatz, in which the final design from the first optimization (see Figure 7a) is used as an initial guess (see Figure 7b). Importantly, the projection parameter β from Equation (18) is reset to one for the second optimization — similarly to how the learning rate is reset, i.e., increased in cosine annealing [105]. The idea of the scheme is summarized by Figure 7.

For transfer learning, a dataset of optimized designs obtained with the linear ansatz is generated. Specifically, the dataset is composed of the initial cost function gradients with respect to the indicator $\partial C / \partial \zeta^{\text{initial}}$, assuming $\zeta^{\text{initial}} = 0$ (see Figures 8a and 8b), and the final designs ζ^{final} (see

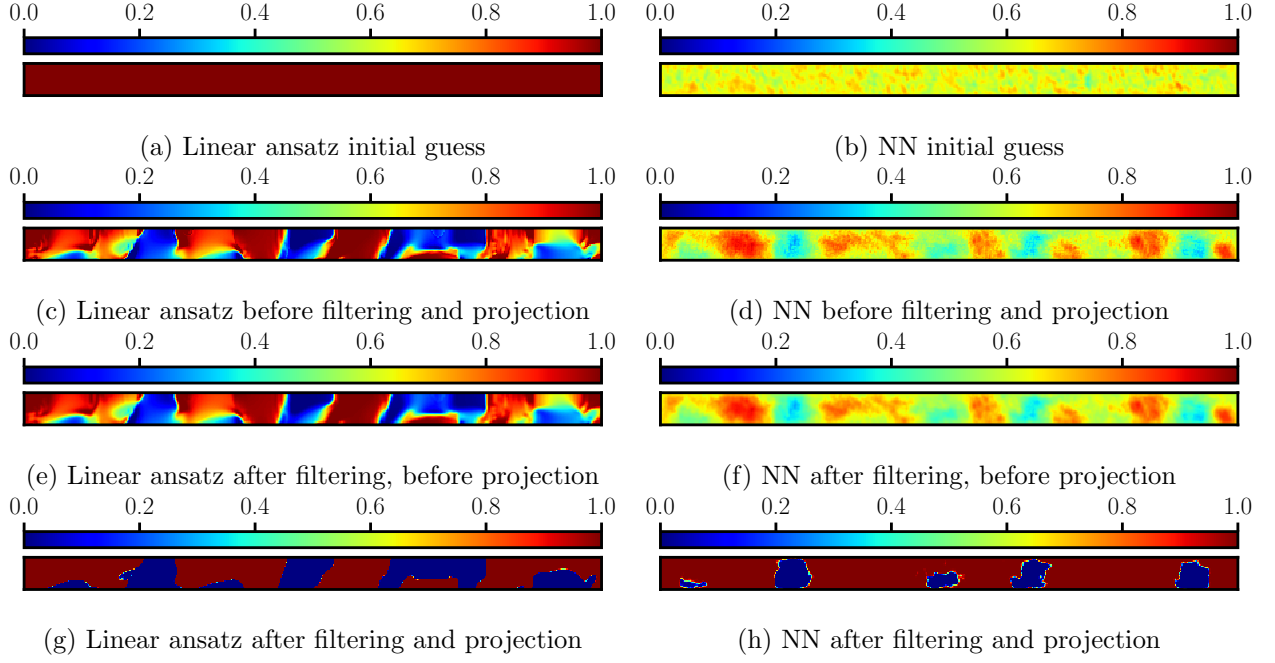


Figure 6: Illustration of the bypassing of the filtering and projection. The sound pressure level at $f = 69.43$ Hz before and after thresholding for the linear ansatz: $L_p^{\text{before}} = 60.22$ dB, $L_p^{\text{after}} = 60.33$ dB; and for the NN ansatz: $L_p^{\text{before}} = 59.88$ dB, $L_p^{\text{after}} = 70.09$ dB

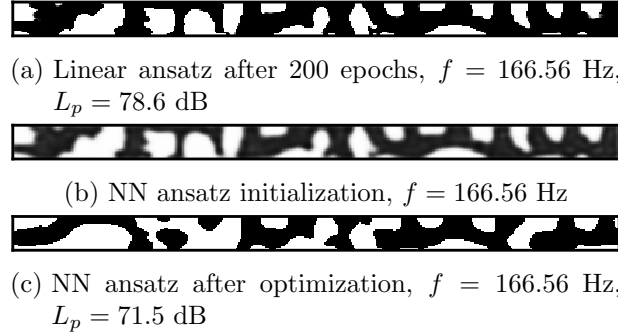


Figure 7: Restarting scheme in which an optimization with linear ansatz is first performed (a), then learned by the NN in a supervised manner (b), and used as an initial guess in a subsequent optimization with the NN ansatz (c)

Figures 8e and 8f). The dataset is generated by sticking to the setup from Figure 1 and randomly sampling the frequency f in the range $[10, 100]$ Hz. Next, the NN is trained in a supervised manner, such that a mapping between $\partial C / \partial \zeta^{\text{initial}}$ and ζ^{final} is established. This step is referred to as pretraining, where the goal is not to obtain an ideal mapping to be used in an online scenario, as in [4–7], but simply a closer qualitative resemblance to material distributions such as those seen in Figures 6c, 6e and 6g. This is illustrated by the prediction of a validation data point in Figure 8c, which demonstrates poor generalization performance compared to the corresponding label in Figure 8f, but a qualitative match with 0/1 designs. This behavior is, therefore, desired, as the target — of the prediction qualitatively matching a 0/1 design — is fulfilled. Only a few data points are required to achieve this, as illustrated with Figure 8 relying on only 4 samples. We experienced the greatest benefit with sample sizes between 4 and 8.

The scheme is demonstrated on two examples with correspondingly $f = 34.39$ Hz and $f = 76.30$ Hz in Figure 9. From the NN initialization obtained through transfer learning (see Figures 9c and 9d), an optimization is performed with the NN ansatz, yielding the designs depicted in Fig-

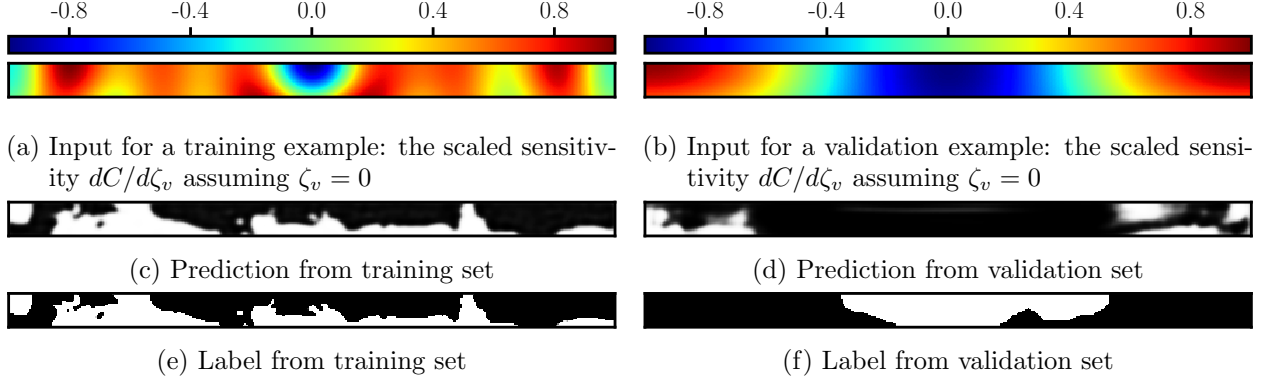


Figure 8: Labeled data for performing the NN pretraining and its corresponding predictions with an NN trained on 4 samples

ures 9e and 9f. As a comparison, optimized designs obtained with a conventional linear ansatz are provided in Figures 9a and 9b.

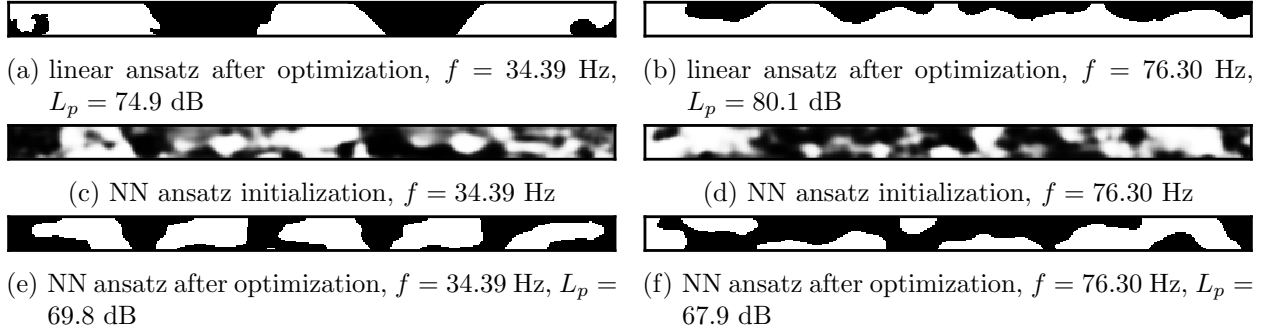


Figure 9: Transfer learning scheme. An NN is pretrained on a number of optimized designs yielding initial guesses (c) and (d). A subsequent optimization leads to the optimized topologies (e) and (f). For reference, the results of a conventional linear ansatz optimization without pretraining is depicted in (a) and (b).

Both schemes were tested extensively, but the transfer learning outperformed the restarting scheme slightly, which is briefly outlined in Appendix E. Therefore, only the pretraining results will be discussed in the following section (Section 4). Both schemes require the additional overhead of pretraining to the linear ansatz and can only be deemed beneficial if better designs are discovered, which would not have been found conventionally.

4. Results

The optimized sound pressure levels will be evaluated on the three stages of optimization described in Appendix B. The first is the sound pressure level after the first 280 epochs obtained with the discretization $q = 2, n_v = 4$, while the second is the sound pressure level obtained from the second optimization with $q = 4, n_v = 4$. The last value stems from the evaluation based on $q = 2, n_v = 1$. This will be presented according to Table 3.

Additionally, the computational effort varies from case to case, captured by the required epochs for tuning initial guesses and learning rates for the first and second optimization. The first optimization always consists of 280 epochs, while the second optimization ranges between 1 and 101 epochs, depending on the number of needed iterations to correct the design due to the initial under-discretization. In addition, a tuning is performed prior to the first optimization. In the

Table 3: Labels of sound pressure levels in upcoming investigations (Tables 4 and 5). The first is the sound pressure level after the first 280 epochs with $q = 2, n_v = 4$, and the second is the sound pressure level after the subsequent optimization with a higher polynomial degree of $q = 4$. Lastly, the optimized design is evaluated on a discretization with $q = 2, n_v = 1$. All designs are thresholded before evaluation.

sound pressure level after first optimization $q = 2, n_v = 4$	sound pressure level after second optimization $q = 4, n_v = 4$	sound pressure level after second optimization $q = 2, n_v = 1$
–	–	–



(a) Seed 1



(b) Seed 2



(c) Seed 3

Figure 10: Three different NN initial guesses for the same optimization problem obtained by changing the NN weight initialization during pretraining (accomplished by modifying the seed)

linear ansatz, three initial guesses: $\zeta = 0, \zeta = 0.5, \zeta = 1$ are compared for 50 epochs of which the best is selected⁷. Similarly, for the NN ansatz, three different initializations are tested by performing three different pretrainings with the same training data but with variations of the NN weight initialization. Three exemplary initial guesses after pretraining are illustrated in Figure 10 reusing the validation data point from Figures 8d and 8f. However, the optimization’s success is also more sensitive to the learning rate when working with the NN ansatz. To this end, also three learning rates: $\alpha = 10^{-5}, \alpha = 2 \cdot 10^{-5}, \alpha = 4 \cdot 10^{-5}$ were compared. This results in $3 \times 3 \times 50 = 450$ tuning epochs for the NN ansatz, yielding an increase in computational effort of about ~ 1.7 per optimization in comparison to the linear ansatz with 150 tuning epochs. Note that the data generation required for the pretraining also comes with a computational overhead, which, relatively seen, is reduced when multiple subsequent optimizations are performed.

4.1. Reference Optimization

To assess if the NN ansatz provides an improvement, a baseline is established with the conventional linear ansatz. The corresponding results are summarized in Table 4 for the eight chosen frequencies.

⁷See Section 4.5 for a statistical evaluation of the initialization’s impact.

Table 4: Reference optimized sound pressure levels with **linear ansatz** using the best result from three initial guesses $\zeta = 0, \zeta = 0.5, \zeta = 1$. Sound pressure levels L_p are given according to the two stages of training and a final evaluation, see Table 3. The epochs consist of the tuning iterations, the first optimization with $q = 2, n_v = 4$, and the second optimization $q = 4, n_v = 4$. The epochs of the second optimization are marked in bold as they vary from case to case and are more expensive.

f	sound pressure level			epochs
21.33 Hz	78.5 dB	79.8 dB	82.2 dB	150 & 280 & 1
34.39 Hz	75.0 dB	75.2 dB	74.9 dB	150 & 280 & 11
57.22 Hz	64.3 dB	62.4 dB	69.1 dB	150 & 280 & 1
69.43 Hz	60.4 dB	61.3 dB	60.5 dB	150 & 280 & 11
76.30 Hz	78.1 dB	78.8 dB	80.1 dB	150 & 280 & 1
95.37 Hz	77.3 dB	79.5 dB	82.9 dB	150 & 280 & 11
141.78 Hz	75.8 dB	78.0 dB	80.5 dB	150 & 280 & 101
166.56 Hz	74.8 dB	75.0 dB	77.8 dB	150 & 280 & 21

4.2. Neural Network Ansatz with Transfer Learning

The same problem is now optimized for the eight frequencies utilizing the transfer learning scheme described in Section 3.2.3 relying on 4 samples during pretraining. The results are summarized by Table 5, where gray highlighting indicates a superiority over the reference obtained in Table 4. The NN yields better optima in all but one case in the optimization phase where $f = 69.43$ Hz poses an exception. During the evaluation, the case with $f = 166.56$ Hz also turns out to be worse. In six out of eight cases, the NN ansatz yields an improvement of correspondingly 12.8 dB, 1.0 dB, 6.4 dB, 11.9 dB, 14.7 dB, and 4.6 dB. Thus, the NN ansatz provides a benefit for determining better optima with a ~ 1.7 higher computational effort.

Interestingly, the designs at higher frequencies — beyond the $f = 100$ Hz threshold employed during pretraining — yield less or no improvement over the reference in Table 4. By modifying the pretraining to incorporate higher frequencies up to $f = 200$ Hz, the designs improve. Thus, the frequency dependency of the designs is relevant for the proposed transfer learning scheme. Further generalization properties are studied in Section 4.4.

Table 5: Optimized sound pressure levels with **NN ansatz** based on **transfer learning** with **4 samples** in the range 10 – 100 Hz. The three sound pressure levels are provided according to Table 3. The gray highlights indicate that the reference from Table 4 is outperformed. Underlining indicates a better design than achieved with transfer learning utilizing a linear ansatz (see Table 6). Additionally, the improvement over the reference designs from Table 4 is quantified.

f	sound pressure level			improvement	epochs
21.33 Hz	<u>63.2 dB</u>	<u>66.8 dB</u>	<u>69.4 dB</u>	12.8 dB	450 & 280 & 1
34.39 Hz	<u>73.1 dB</u>	<u>73.5 dB</u>	<u>73.9 dB</u>	1.0 dB	450 & 280 & 1
57.22 Hz	<u>54.6 dB</u>	<u>60.0 dB</u>	<u>62.7 dB</u>	6.4 dB	450 & 280 & 1
69.43 Hz	64.7 dB	64.1 dB	66.6 dB	-6.1 dB	450 & 280 & 31
76.30 Hz	<u>74.3 dB</u>	<u>75.2 dB</u>	<u>68.2 dB</u>	11.9 dB	450 & 280 & 1
95.37 Hz	<u>72.4 dB</u>	<u>72.2 dB</u>	<u>68.2 dB</u>	14.7 dB	450 & 280 & 11
141.78 Hz	69.4 dB	69.8 dB	<u>75.9 dB</u>	4.6 dB	450 & 280 & 41
166.56 Hz	<u>73.1 dB</u>	<u>74.2 dB</u>	<u>78.5 dB</u>	-0.7 dB	450 & 280 & 21

4.3. Neural Network Prediction as Initial Guess for Linear Ansatz

Naturally, the question arises of whether it is truly the NN that is beneficial or only the initial guess provided through the pretraining. To this end, we isolate the effect of the pretraining. Instead of relying on the NN ansatz during the optimization, a linear ansatz is employed but initialized with the initial guess of the pretrained NN. With the same pretraining as employed for Table 5, an optimization with the linear ansatz and initial NN guess results in Table 6. As seen by the gray highlights, only half of the investigated cases provide an improvement over the reference from Table 4. Furthermore, the underlined sound pressure level values in Table 5 and Table 6 indicate a better attained optimum with the respective method. The linear ansatz with an NN initial guess only yields a better design for one case, $f = 141.78$ Hz, which, however, turns out to be worse during the final evaluation with $q = 2, n_v = 1$.

Table 6: Optimized sound pressure levels with **linear ansatz** using **transfer learning** with **4 samples** in the range 10 – 100 Hz to provide an initial guess. The three sound pressure levels are provided according to Table 3. The gray highlights indicate that the reference from Table 4 is outperformed. Underlining indicates a better design than achieved with transfer learning utilizing a linear ansatz (see Table 5). Additionally, the improvement over the reference designs from Table 4 is quantified.

f	sound pressure level			improvement	epochs
21.33 Hz	82.4 dB	84.2 dB	85.0 dB	-2.8 dB	450 & 280 & 1
34.39 Hz	74.6 dB	75.8 dB	76.6 dB	-1.7 dB	450 & 280 & 1
57.22 Hz	62.3 dB	60.2 dB	68.9 dB	0.2 dB	450 & 280 & 11
69.43 Hz	71.9 dB	72.0 dB	73.7 dB	-13.2 dB	450 & 280 & 11
76.30 Hz	75.2 dB	75.4 dB	80.1 dB	0.0 dB	450 & 280 & 21
95.37 Hz	71.1 dB	65.1 dB	81.4 dB	1.5 dB	450 & 280 & 101
141.78 Hz	<u>59.9 dB</u>	<u>67.3 dB</u>	76.8 dB	3.7 dB	450 & 280 & 101
166.56 Hz	73.4 dB	75.3 dB	82.7 dB	-4.9 dB	450 & 280 & 101



(a) Linear ansatz after optimization, $f = 57.22$ Hz, $L_p = 68.9$ dB



(b) NN ansatz after optimization, $f = 57.22$ Hz, $L_p = 62.7$ dB



(c) Linear ansatz after optimization, $f = 166.56$ Hz, $L_p = 82.7$ dB



(d) NN ansatz after optimization, $f = 166.56$ Hz, $L_p = 78.5$ dB

Figure 11: Optimized topologies using transfer learning based on 8 samples with the linear ansatz on the left and the NN ansatz on the right

The cost histories over the epochs are illustrated in Figure 12 for correspondingly the best performance achieved with an NN, i.e., $f = 95.37$ Hz, and the worst performance, i.e., $f = 69.43$ Hz (compare Table 5 with Table 4). Figure 12a shows the histories of the pretrained NN ansatz compared to the reference trajectories with a linear ansatz, while Figure 12a depicts the trajectories of the linear ansatz with and without initial guess provided by the NN.

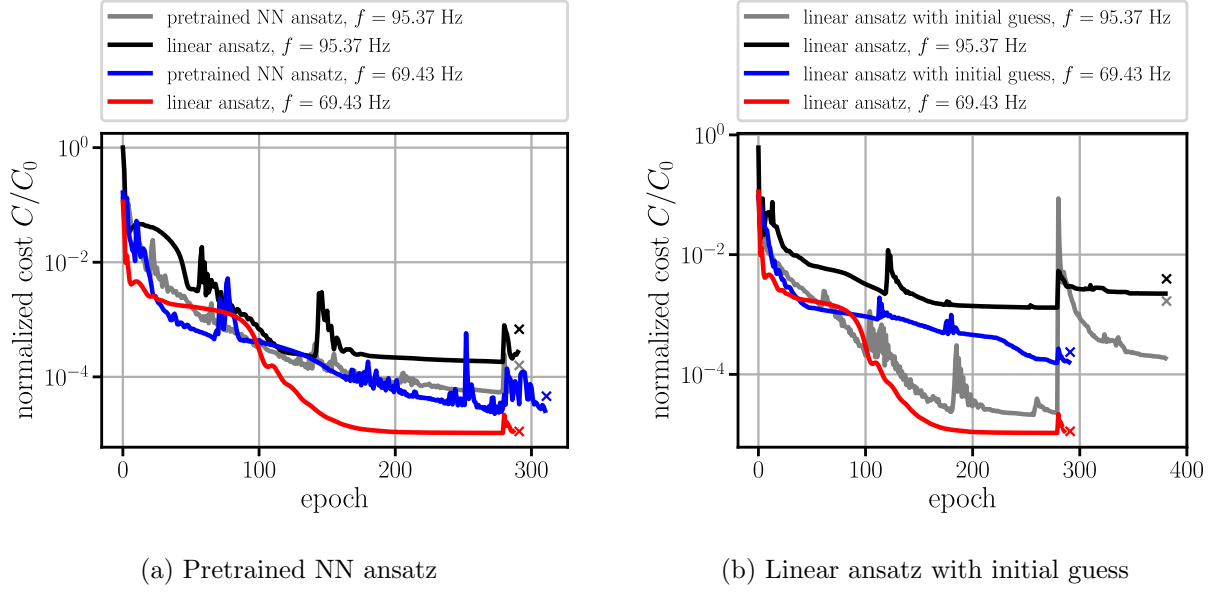


Figure 12: Cost histories of the best and worst cases of the transfer learning scheme based on 4 samples for correspondingly the NN and linear ansatz. The final correctly evaluated cost functions are indicated by the crosses. The curves with the linear ansatz (without initial guess) are provided as reference and are identical in (a) and (b).

4.4. Generalization

As a final investigation, the generalization capabilities of transfer learning are investigated — in order to evaluate if a new pretraining is necessary for a change in problem setup (see Figure 1) beyond the change in frequency. To this end, the same pretraining is employed for a novel setup characterized by the changes in Table 7. The source is moved closer to the ceiling and relocated to the right side of the domain, while the domain to be suppressed is reduced in size and shifted to the left.

Table 7: Modified dimensions of the problem. Compare to Table 1 and the problem setup in Figure 1. Dimensions are provided in meters.

x_f	y_f	x_s	y_s	a_s	b_s
17	6	5.5	6.5	1	1

The optimization is performed with a pretraining using 4 and 8 samples. A comparison with designs obtained with the conventional linear ansatz is provided in Figure 13. For the NN ansatz, the best of the two pretrainings is illustrated. The pretraining with 4 samples consistently outperforms the linear ansatz for every tested frequency, while with 8 samples, the linear ansatz remains superior for $f = 69.43$ Hz, $f = 141.78$ Hz, and $f = 166.56$ Hz. However, the extent to which the linear ansatz designs are surpassed is impressive. When choosing the best of the two NN pretrainings, the improvements are 13.6 dB, 24 dB, 10.1 dB, 2.1 dB, 29.6 dB, 22.8 dB, 1.4 dB, and 1.9 dB. Thus, a single pretraining can be reused for different problem setups, rendering the relative cost of the pretraining negligible.

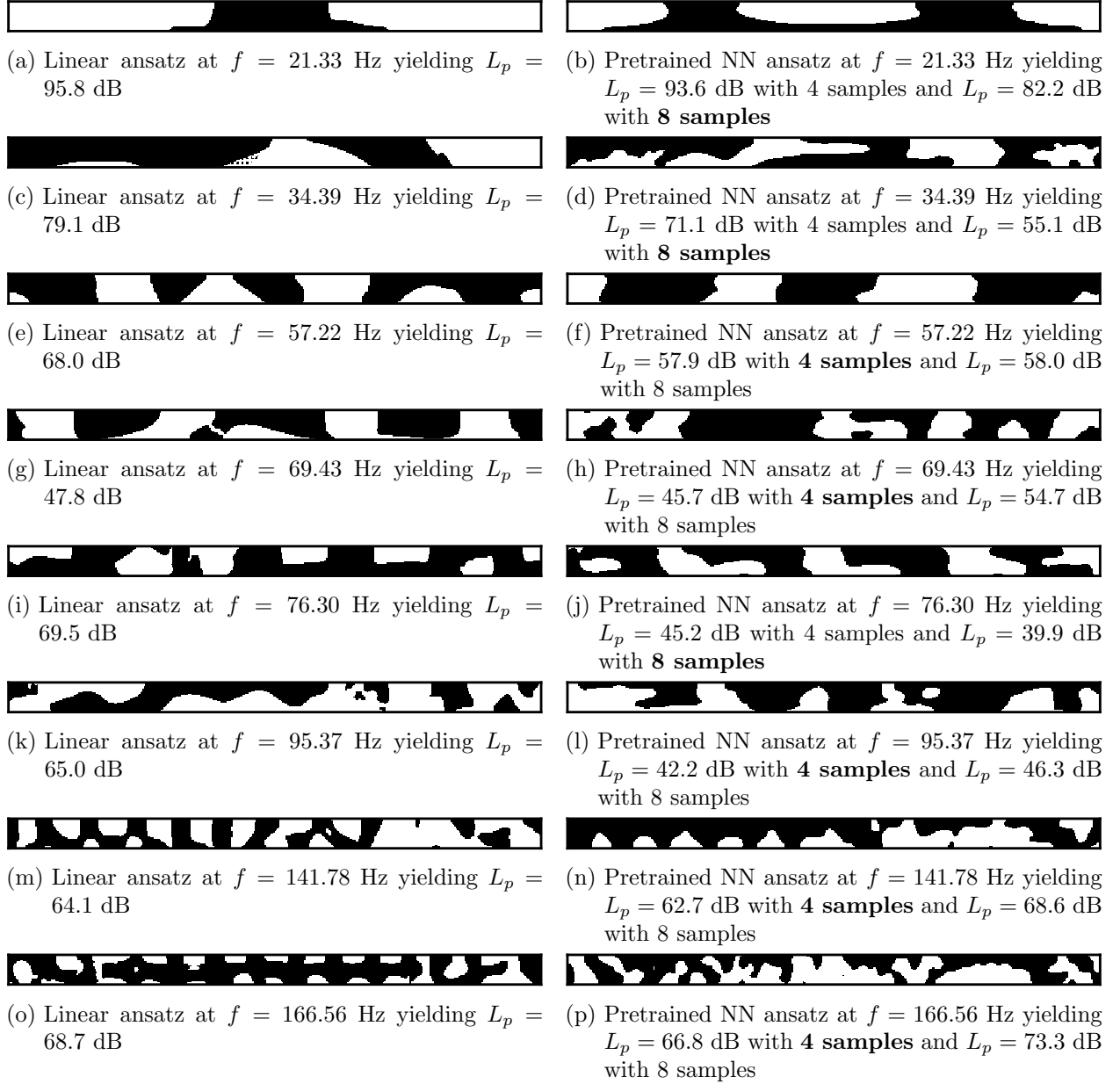


Figure 13: Optimized topologies for the adapted problem using transfer learning based on 4 or 8 samples with the NN ansatz on the right. The best possible design is depicted and indicated in bold. The left depicts optimized topologies without pretraining using a linear ansatz, i.e., the conventional approach.

4.5. Statistical Evaluation

To complete the previous analysis, a statistical assessment of the initialization's effect on the two ansatz' is provided. The question is: does the NN consistently find better optima or are the observed advantages singular results discovered by chance? To this end, the generalization case from Section 4.4 is reconsidered. Instead of searching for the best initialization from three possibilities, separate optimizations are performed with 30 different initializations for each frequency. In the linear case, 30 homogeneous initial guesses are considered in the range $[0, 1]$, while for the NN ansatz, 30 different pretrainings with the same four data samples are performed. The resulting distributions are represented as histograms in Figure 14 for the frequencies $f = 21.33$ Hz, $f = 57.22$ Hz, $f = 76.30$ Hz, and $f = 95.37$ Hz. The remaining histograms are provided in Appendix F. The sound pressure levels achieved with the NN ansatz are indicated in blue, while red marks those obtained using the linear ansatz. For $f = 21.33$ Hz and $f = 57.22$ Hz, given in Figures 14a and 14b,

the distributions mostly overlap. However, in both cases, the best designs are obtained with the NN — and in Figure 14a, outliers in the NN distribution represent an improvement of ~ 10 dB over the linear ansatz. Figures 14c and 14d with $f = 76.30$ Hz, and $f = 95.37$ Hz demonstrate a clear separation in design quality distribution. This also corresponds to the cases in Figure 13 with the greatest improvement through an NN ansatz. The overlaps of the distributions are minimal, and in these scenarios, the NN ansatz consistently outperforms the linear ansatz. Thus, it can be concluded that the obtainable improvement through an NN ansatz is highly problem-dependent. Furthermore, initializations superior to the homogeneous initialization might also mitigate the NN’s advantage. However, using the same NN initializations for the linear ansatz was not beneficial, as seen in Section 4.3, strengthening the potential of an NN ansatz.

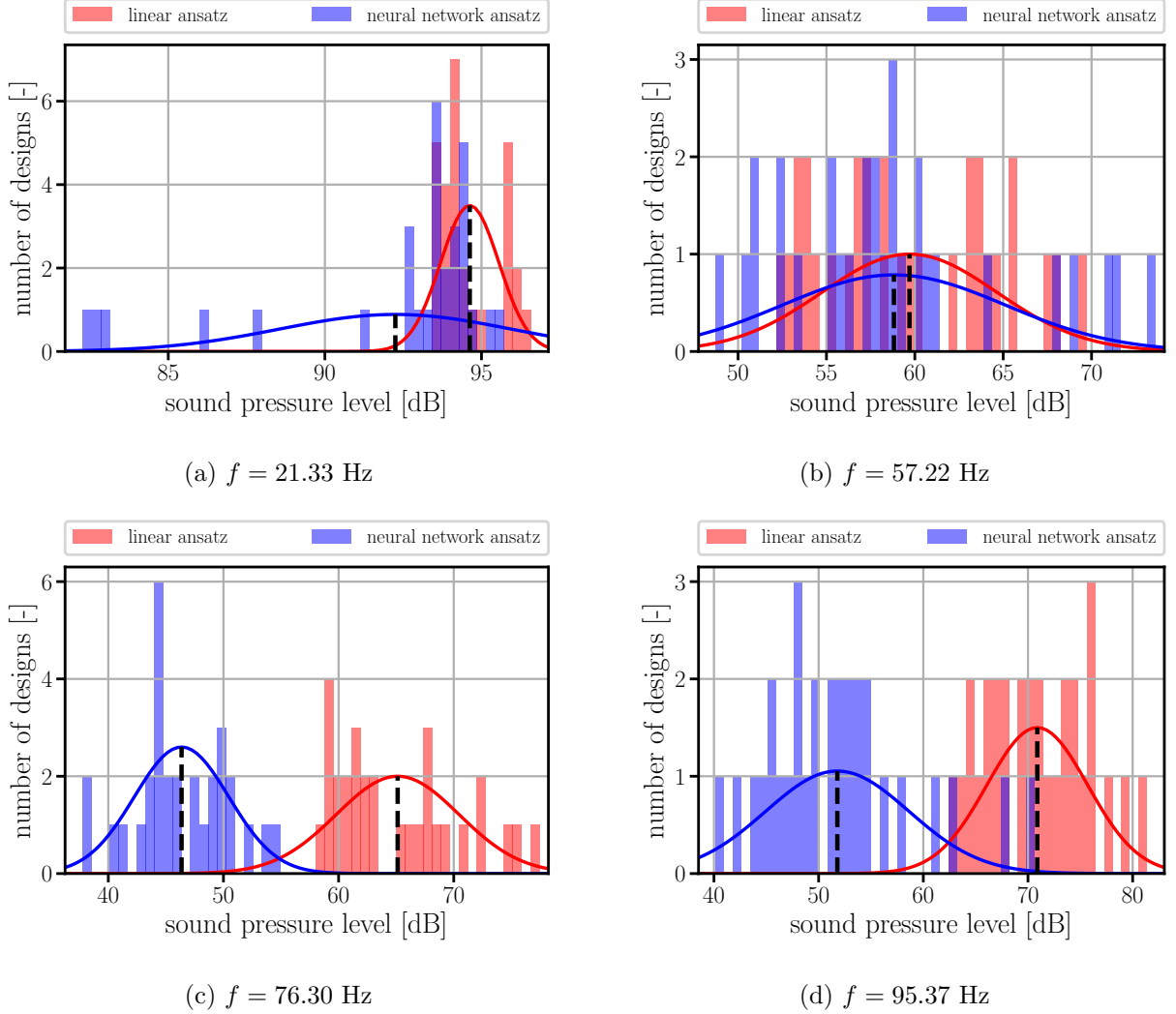


Figure 14: Statistical evaluation of the local optima quality with 30 samples for the linear (with homogeneous initial guesses) and the pretrained NN ansatz — relying on different initializations. In the linear case, we used 30 homogeneous initial guesses equally spaced between 0 and 1, while the NN relies on 30 different pretrainings.

5. Conclusion

This work investigates the usefulness of material parameterizations with NNs in the context of topology optimization on the specific problem of acoustic topology optimization. It is found that a pretrained NN relying on the concept of transfer learning is often able to identify better local

optima, i.e., better designs than classical parameterizations. The origin of the benefit is currently not clear and has to be investigated further, as recently initiated by [106]. A possible explanation is that the overparametrization of the design variables decreases the chances of all gradient components becoming zero, i.e., getting stuck in a local optimum prematurely. Furthermore, similar results could possibly be reached by classical methods, such as the use of larger filters in the initial design stages to convexify the design problem [107] and thereby avoid premature convergence. Considering the adjustment of parameters of the first NN layers as comparable to larger filters could be another explanation as to why the neural network ansatz is beneficial.

However, without convexification or other classical tuning efforts, finding a better optimum is often possible in the investigated acoustic topology optimization cases — but still not guaranteed. The chances of finding one are increased by performing multiple optimizations with different NN initializations.

The NN ansatz is only found to be advantageous in combination with the first-order optimizer Adam, which was demonstrated with the Rosenbrock function, as a benchmark. It was also found that the presented method is currently incompatible with constrained optimizers, such as optimality criteria methods or the method of moving asymptotes. The obstacle is that concrete design variable updates can not directly be transferred to the NN parametrization but only update directions in terms of gradients. Until now, the constraints in the compliance problem have been addressed through penalty constraints [54–57]. To make the NN ansatz truly viable in topology optimization, the incorporation of constraints would have to be improved.

However, NN material parametrizations show some potential for acoustic topology optimization and could benefit other unconstrained optimization problems⁸. Significantly better optima were identified with comparable computational efforts — which were less than twice as large.

Acknowledgements

We gratefully acknowledge the funds received by the Georg Nemetschek Institut (GNI) under the project Deep-Monitor. Furthermore, Ole Sigmund was supported by the Villum Investigator Project AMSTRAD (VIL54487) from VILLUM FONDEN.

Declarations

Conflict of interest No potential conflict of interest was reported by the authors.

Data Availability

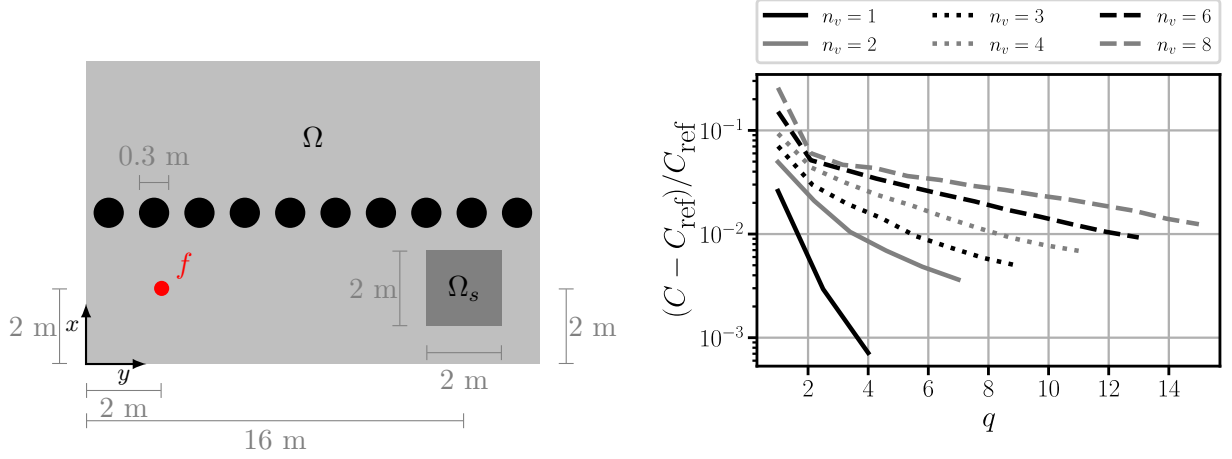
We provide a PyTorch [95] implementation of all methods in [108].

A. High-Order Multi-Resolution Acoustic Topology Optimization

High-order multi-resolution topology optimization has previously been performed for the compliance problem in [82], where speedups of ~ 3 in two dimensions and of ~ 32 in three dimensions were obtained. Investigations for other problems have been limited. To reduce the computational effort of the acoustic topology optimization, we employ a high-order multi-resolution discretization. To this end, a brief investigation is performed. Before delving into an optimization, a convergence study for different polynomial degrees q and number of subvoxels n_v is performed. For this, the problem depicted in Figure 15a is considered with air throughout the entire domain Ω , except the

⁸where [106] emphasize that the potential lies in non-convex optimization problems. Applying neural network reparametrizations to convex optimization slows convergence.

circular inclusions, indicated in black. The number of total voxels is kept fixed with 432×216 voxels as described in Section 2.2. The considered frequency is $f = 34.39$ Hz. The quantity of interest is the cost function C defined as in Equation (10). A high-fidelity solution with $q = 4, n_v = 1$ is used as reference C_{ref} . From Figure 15b, it becomes apparent that more subvoxels decrease the solution quality. However, keep in mind that more subvoxels also decrease the number of degrees of freedom drastically without decreasing the number of design variables.



(a) Problem setup within the $18 \text{ m} \times 9 \text{ m}$ domain with $\zeta = 0$ in Ω and $\zeta = 1$ in the centered black circles

(b) Convergence for $f = 34.39$ Hz

Figure 15: High-order multi-resolution convergence study

To quantify the impact of potentially under-discretizing the problem, optimizations are to be conducted for different discretizations. To this end, we consider two frequencies $f = 69.43$ Hz and $f = 34.39$ Hz on the setup from Figure 1 with dimensions from Table 1. For each discretization, the final design is to be tested on a more accurate discretization, which is chosen as $q = 2, n_v = 1$, thus incurring a relative error of less than 1% according to Figure 15b. Three quantities of interest are established:

- the normalized speed-up of the simulation, where standard linear finite element, i.e., $q = 1, n_v = 1$ is taken as reference,
- the cost increase after adapting the discretization to $q = 2, n_v = 1$,
- and the final sound pressure level in dB evaluated with $q = 2, n_v = 1$.

Note that the design is not thresholded to compute the final sound pressure level to isolate the effect of the change in discretization. As these quantities are obtained for two frequencies, six values are computed for each discretization and arranged according to Table 8. The optimization is conducted for 300 epochs using a filter radius twice the voxel size.

Table 8: Labels of Tables 9 and 10. Normalization with respect to time and cost is obtained with $q = 1, n_v = 1$.

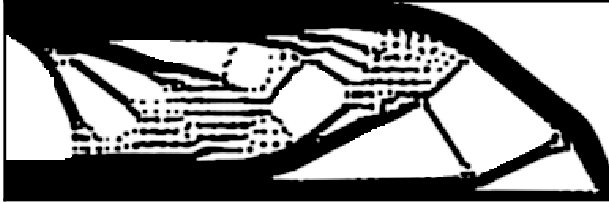
	normalized speed-up	cost increase after the discretization change	corrected sound pressure level in dB
$f = 69.43$ Hz	—	—	—
$f = 34.39$ Hz	—	—	—

The corresponding results are presented in Table 9, where equal performances and improvements in comparison to the discretization $q = 1, n_v = 1$ are highlighted in gray. Thus, any normalized speed-up ≥ 1 , any cost increase ≤ 1.5 , and any design ≤ 65 dB and ≤ 78 dB (within 5% of the design obtained with $q = 1, n_v = 1$) is highlighted. Considering this, only minor improvements can be expected with maximal speed-ups of ~ 3 using $q = 2, n_v = 3$.

Table 9: Normalized time, cost increase after discretization change, and corrected sound pressure level (see Table 8) for different discretizations relying on 432×216 voxels at $f = 69.43$ Hz and $f = 34.39$ Hz

	$n_v = 1$			$n_v = 2$			$n_v = 3$			$n_v = 4$			$n_v = 6$			$n_v = 8$		
$q = 1$	1	1.5	62	4.7	2.6	69	—			—			—			—		
	1	1	75	4.8	1.3	76												
$q = 2$	—			1.1	1.4	62	3.3	1.5	62	6.9	3.6	66	17.1	40.9	81	29.9	41.1	81
				1.1	1.1	75	3.3	1.2	75	7.3	11.0	85	17.4	15.2	87	30.4	7.0	83
$q = 3$	—			—			1.4	1.5	62	2.9	1.7	63	3.7	6.4	72	13.5	6.9	73
							1.4	1.1	75	2.9	1.5	77	7.2	14.7	87	13.6	9.1	84
$q = 4$	—			—			—			1.3	1.5	62	3.2	1.6	66	6.1	6.0	74
										1.3	1	75	3.2	2.4	79	6.0	20.1	88
$q = 5$	—			—			—			—			1.7	1.5	66	3.1	1.8	67
													1.7	3.2	80	3.0	2.8	79
$q = 6$	—			—			—			—			—			1.6	6.3	73
																1.6	2.7	79

However, in contrast to the compliance problem, in which severe artifacts occur when under-discretizing [82] (see Figure 16a), such artifacts seem rare and localized in acoustic topology optimization. One of these rare examples, hand-selected from many other under-discretized optimizations that did not show these artifacts, is provided in Figure 16b.



(a) Artifacts in compliance problem



(b) Artifacts in acoustic problem at $f = 34.39$ Hz

Figure 16: Numerical artifacts due to under-discretization in high-order multi-resolution topology optimization achieved with $q = 1, n_v = 4$, and a filter radius twice the voxel size

Due to the localization and rarity of these artifacts, the question arises of how far the designs obtained with under-discretizations are from useful designs. To answer this question, a second optimization is to be performed subsequent to the under-discretized optimization. Specifically, the first discretization is performed for 280 epochs, followed by a second for 20 epochs where the polynomial degree has been increased by two. Similar to before, the quantities of interest from Table 8 are evaluated for the adapted optimization scheme in Table 10. Again, equal performances and improvements in comparison to the discretization $q = 1, n_v = 1$ are highlighted in gray. Thus, any normalized speed-up ≥ 1 , any cost increase ≤ 1.5 , and any design ≤ 65 dB and ≤ 78 dB (considering the same baseline as for Table 9) is highlighted. With this modification, the advantages of a high-order multi-resolution discretization become more prominent. The discretization $q = 2, n_v = 4$ yields consistent results with a speed-up of ~ 5 and is therefore employed throughout the remainder of this work.

Table 10: Normalized time, cost increase after discretization change, and corrected sound pressure level (see Table 8) for different discretizations relying on 432×216 voxels at $f = 69.43$ Hz and $f = 34.39$ Hz utilizing the proposed correction scheme with a second higher-order optimization

	$n_v = 1$			$n_v = 2$			$n_v = 3$			$n_v = 4$			$n_v = 6$			$n_v = 8$		
$q = 1$	0.9	1.2	61	3.4	1.1	70	6.2	1.0	83	9.8	1.0	83	11.6	1.0	82	15.2	1.0	82
	1.0	1.1	75	4.0	1.2	76	5.4	1.2	76	8.5	1.1	75	12.2	1.0	75	13.0	1.0	85
$q = 2$	–			0.9	1.3	61	2.5	1.3	61	4.6	1.1	61	8.1	1.6	67	11.9	1.2	69
				1.1	1.3	76	2.9	1.1	75	5.2	1.1	75	9.2	1.3	76	11.7	1.0	75
$q = 3$	–			–			1.2	1.3	62	2.2	1.2	61	4.9	1.1	68	8.1	1.7	67
							1.3	1.3	76	2.6	1.2	76	5.4	1.1	75	8.1	1.0	76
$q = 4$	–			–			–			1.1	1.4	62	2.4	1.3	65	4.8	1.3	68
										1.2	1.0	75	2.8	1.2	76	4.7	1.9	78
$q = 5$	–			–			–			–			1.4	1.3	65	2.7	1.4	66
													1.6	2.0	78	2.7	0.9	75
$q = 6$	–			–			–			–			–			1.3	3.1	70
																1.5	1.2	76

Figure 17 provides a visualization of the proposed two-step optimization scheme for $f = 34.39$ Hz and $f = 69.43$ Hz using $q = 2, n_v = 4$. The change introduced by the second optimization is visualized in Figures 17c and 17d, where red indicates material removal, while blue shows additional material. Thus, only minor changes are needed. The cost histories for the two cases are illustrated in Figure 18, where the dashed line indicates the point at which the discretization is changed from $q = 2, n_v = 4$ to $q = 4, n_v = 4$. Only a few iterations are needed to amend the errors introduced by the under-discretization.

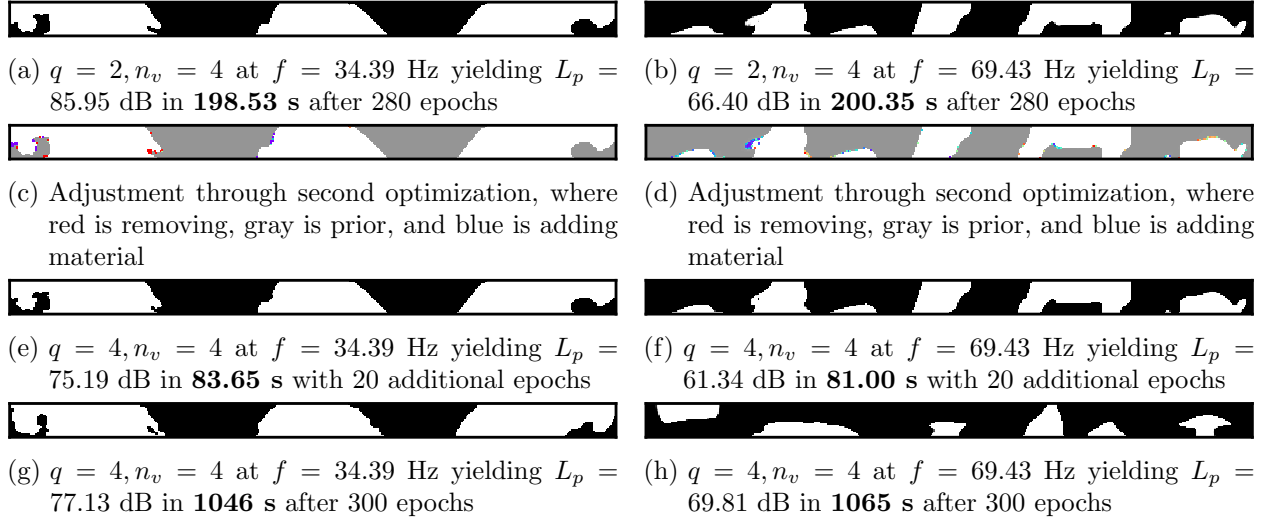


Figure 17: Ensuring good optima despite under-discretization going from $n_v = 4, q = 2$ to $n_v = 4, q = 4$

B. Two-Dimensional Optimization Benchmarks

Aside the Rosenbrock function from Equation (19), the Rastrigrin function

$$f(x, y) = 20 + x^2 - 10 \cos(2\pi x) + y^2 - 10 \cos(2\pi y), \quad (21)$$

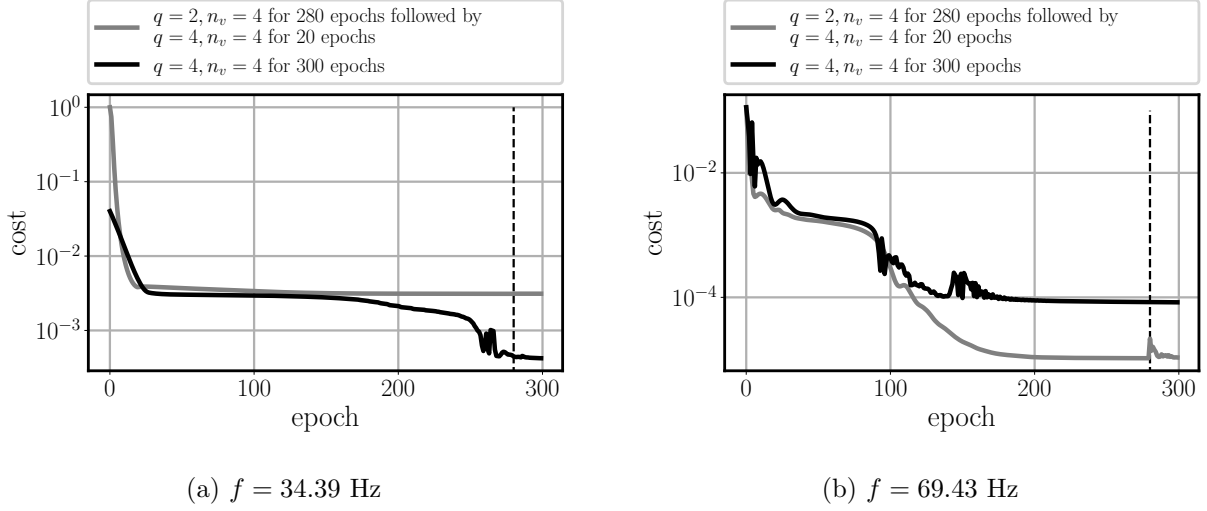


Figure 18: Comparison of cost histories in high-order multi-resolution acoustic topology optimization. Black indicates a conventional optimization obtained after 300 epochs with $q = 4, n_v = 4$, while gray showcases the result using the proposed two-step optimization scheme, where a switch from $q = 2, n_v = 4$ to $q = 4, n_v = 4$ is made at epoch 280.

the Ackley function

$$f(x, y) = -20e^{-0.2\sqrt{0.5(x^2+y^2)}} - e^{0.5(\cos(2\pi x) + \cos(2\pi y))} + e + 20, \quad (22)$$

and the Lévi function

$$f(x, y) = \sin^2(3\pi x) + (x - 1)^2(1 + \sin^2(3\pi y)) + (y - 1)^2(1 + \sin^2(2\pi y)) \quad (23)$$

are considered. The corresponding optimization landscapes are depicted in Figure 19 with the global minima indicated by white squares.

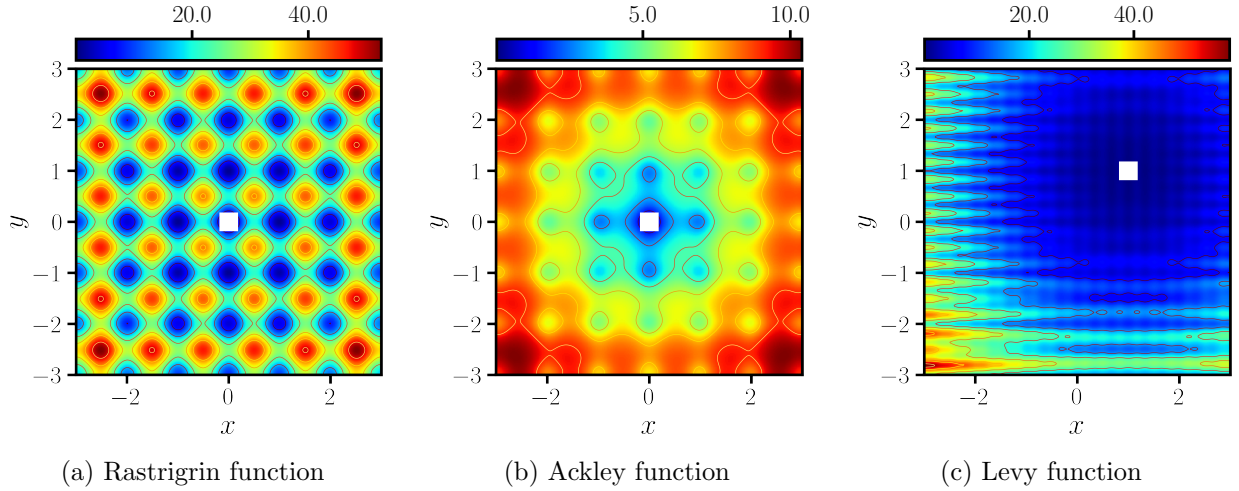


Figure 19: Two-dimensional optimization landscapes with the global minima indicated by white squares

C. Natural Frequency Estimation

For the natural frequency estimation of the undisturbed domain, the nm th wavefield $\hat{p}(x, y)$ with the form of

$$\hat{p} = \hat{p}_0 \cos\left(\frac{n\pi x}{a}\right) \cos\left(\frac{m\pi y}{b}\right) \quad (24)$$

is assumed, which fulfills the homogeneous Neumann boundary conditions. Inserting Equation (24) into the homogeneous version of the Helmholtz equation from Equation (4) and assuming a homogeneous material distribution of $\tilde{\kappa} = 1$ and $\tilde{\rho} = 1$, i.e., assuming air everywhere, yields an expression for the nm th frequency f_{nm} .

$$f_{nm} = \frac{\omega_{nm}}{2\pi} = \frac{\tilde{\omega}_{nm}c_1}{2\pi} \frac{c_1}{2} \sqrt{\left(\frac{n}{L_x}\right)^2 + \left(\frac{m}{L_y}\right)^2} \quad (25)$$

The wave speed of air c_1 is defined with the material parameters of air.

$$c_1 = \sqrt{\kappa_1/\rho_1} \quad (26)$$

D. Neural Network Architecture

The employed NN is a U-net [109] with three downsampling and three upsampling blocks. It consists of 148 806 trainable parameters and is summarized by Table 11. The input to the NN is always the cost function gradient with respect to the indicator $\partial C/\partial \zeta$, assuming $\zeta = 0$ in the entire domain Ω . This input choice was first proposed in [60] in the context of full waveform inversion. For further details, the interested reader is referred to the code made available in [108].

Table 11: Two-dimensional U-net [109] constructed with convolutional NNs for the prediction of the filtered and projected indicator $\tilde{\zeta}$. The total number of trainable parameters is 148 806.

layer	shape after layer	learnable parameters
input	$1 \times 432 \times 24$	0
downsampling		
max pooling	$1 \times 216 \times 12$	0
batch norm	$1 \times 216 \times 12$	2
convolution & leaky ReLU	$12 \times 216 \times 12$	312
max pooling	$12 \times 108 \times 6$	0
batch norm	$12 \times 108 \times 6$	24
convolution & leaky ReLU	$24 \times 108 \times 6$	7 224
max pooling	$24 \times 54 \times 3$	0
batch norm	$24 \times 54 \times 3$	48
convolution	$48 \times 54 \times 3$	28 848
bottleneck		
batch norm	$48 \times 54 \times 3$	96
convolution & leaky ReLU	$48 \times 54 \times 3$	57 648
upsampling		
upsample & skip connection	$72 \times 108 \times 6$	0
batch norm	$72 \times 108 \times 6$	144
convolution & leaky ReLU	$24 \times 108 \times 6$	43 224
upsample & skip connection	$36 \times 216 \times 12$	0
batch norm	$36 \times 216 \times 12$	72
convolution & leaky ReLU	$12 \times 216 \times 12$	10 812
upsample & skip connection	$13 \times 432 \times 24$	0
batch norm	$13 \times 432 \times 24$	26
convolution & Sigmoid	$1 \times 432 \times 24$	326
filtering	$1 \times 432 \times 24$	0
projection	$1 \times 432 \times 24$	0

E. Evaluation of Restarting Scheme

The sound pressure levels achieved with the optimized designs using the restarting scheme and the NN ansatz are summarized in Table 12. Comparing the results from the transfer learning scheme in Table 5, transfer learning arises as the slightly superior approach. In three of the eight cases, the restarting scheme produces better designs, indicated in dark gray in Table 12. However, the transfer learning scheme bears the additional advantage of only requiring a single pretraining for many subsequent optimizations, while the restarting scheme needs one initial optimization for each run.

Table 12: Optimized sound pressure levels with **NN ansatz** based on the **restarting scheme**. The first sound pressure level is from the initial optimization (i.e., before the restart), while the latter three are as described in Table 3. The gray highlights indicate that the reference from Table 4 is outperformed. Additionally, the improvement over the reference designs from Table 4 is quantified, where the dark gray highlights indicate better designs than those obtained with transfer learning in Table 5.

f	sound pressure level				improvement	epochs
21.33 Hz	78.5 dB	79.2 dB	73.5 dB	78.3 dB	3.9 dB	150 & 300 & 21
34.39 Hz	75.2 dB	72.5 dB	73.5 dB	74.5 dB	0.4 dB	150 & 300 & 1
57.22 Hz	61.6 dB	51.6 dB	52.5 dB	56.1 dB	13.0 dB	150 & 300 & 21
69.43 Hz	60.4 dB	58.8 dB	59.9 dB	62.3 dB	-1.8 dB	150 & 280 & 11
76.30 Hz	78.3 dB	71.6 dB	73.3 dB	75.2 dB	4.9 dB	150 & 300 & 1
95.37 Hz	70.0 dB	63.2 dB	66.6 dB	78.3 dB	4.6 dB	150 & 300 & 31
141.78 Hz	79.6 dB	76.8 dB	77.7 dB	79.2 dB	1.3 dB	150 & 300 & 1
166.56 Hz	78.6 dB	70.0 dB	70.1 dB	71.5 dB	6.3 dB	150 & 300 & 11

F. Additional Statistical Evaluations

For the sake of completeness, the remaining histograms from Section 4.5 are provided in Figure 20 for frequencies $f = 34.39$ Hz, $f = 69.43$ Hz, $f = 141.78$ Hz, and $f = 166.56$ Hz.

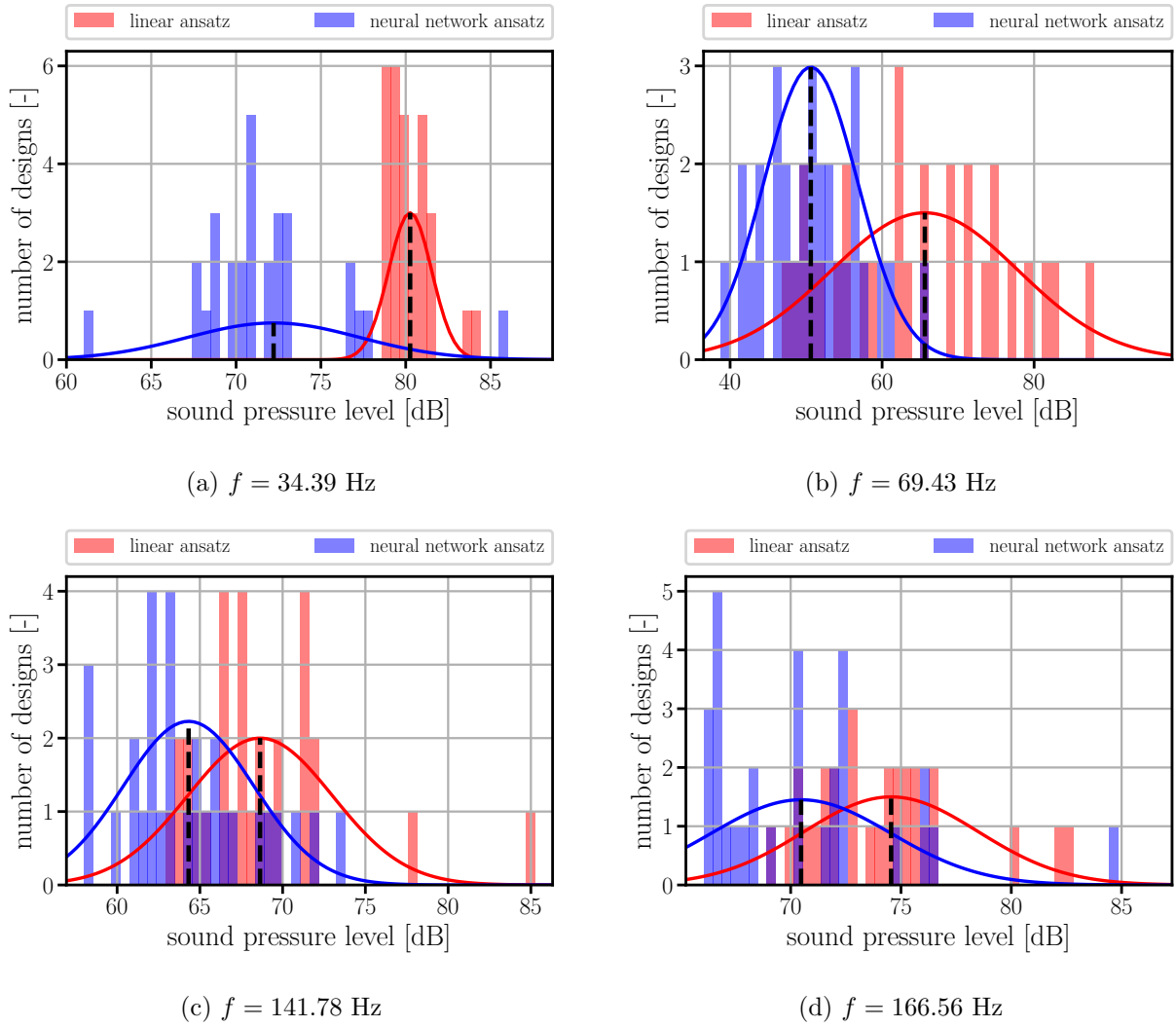


Figure 20: Statistical evaluation of the local optima quality with 30 samples for the linear (with homogeneous initial guesses) and the pretrained NN ansatz — relying on different initializations. In the linear case, we used 30 homogeneous initial guesses equally spaced between 0 and 1, while the NN relies on 30 different pretrainings.

References

- [1] Ian Goodfellow, Yoshua Bengio, and Aaron Courville. *Deep Learning*. MIT Press, 2016. ISBN 0-262-03561-8. URL <http://www.deeplearningbook.org>.
- [2] Rebekka V. Woldseth, Niels Aage, J. Andreas Bærentzen, and Ole Sigmund. On the use of artificial neural networks in topology optimisation. *Structural and Multidisciplinary Optimization*, 65(10):294, October 2022. ISSN 1615-1488. doi: 10.1007/s00158-022-03347-1. URL <https://doi.org/10.1007/s00158-022-03347-1>.
- [3] Leon Herrmann and Stefan Kollmannsberger. Deep learning in computational mechanics: a review. *Computational Mechanics*, January 2024. ISSN 0178-7675, 1432-0924. doi: 10.1007/s00466-023-02434-4. URL <https://link.springer.com/10.1007/s00466-023-02434-4>.
- [4] Diab W. Abueidda, Seid Koric, and Nahil A. Sobh. Topology optimization of 2D structures with nonlinearities using deep learning. *Computers & Structures*, 237:106283, September 2020. ISSN 0045-7949. doi: 10.1016/j.compstruc.2020.106283. URL <https://www.sciencedirect.com/science/article/pii/S0045794920300869>.
- [5] Shuai Zheng, Zhenzhen He, and Honglei Liu. Generating three-dimensional structural topologies via a U-Net convolutional neural network. *Thin-Walled Structures*, 159:107263, February 2021. ISSN 0263-8231. doi: 10.1016/j.tws.2020.107263. URL <https://www.sciencedirect.com/science/article/pii/S0263823120311319>.
- [6] Dalei Wang, Cheng Xiang, Yue Pan, Airon Chen, Xiaoyi Zhou, and Yiquan Zhang. A deep convolutional neural network for topology optimization with perceptible generalization ability. *Engineering Optimization*, 54(6):973–988, June 2022. ISSN 0305-215X, 1029-0273. doi: 10.1080/0305215X.2021.1902998. URL <https://www.tandfonline.com/doi/full/10.1080/0305215X.2021.1902998>.
- [7] Jun Yan, Qi Zhang, Qi Xu, Zhirui Fan, Haijiang Li, Wei Sun, and Guangyuan Wang. Deep learning driven real time topology optimisation based on initial stress learning. *Advanced Engineering Informatics*, 51:101472, 2021.

January 2022. ISSN 1474-0346. doi: 10.1016/j.aei.2021.101472. URL <https://www.sciencedirect.com/science/article/pii/S1474034621002226>.

- [8] Gorkem Can Ates and Recep M. Gorguluarslan. Two-stage convolutional encoder-decoder network to improve the performance and reliability of deep learning models for topology optimization. *Structural and Multidisciplinary Optimization*, 63(4):1927–1950, April 2021. ISSN 1615-1488. doi: 10.1007/s00158-020-02788-w. URL <https://doi.org/10.1007/s00158-020-02788-w>.
- [9] Jiaxiang Luo, Yu Li, Weien Zhou, Zhiqiang Gong, Zeyu Zhang, and Wen Yao. An Improved Data-Driven Topology Optimization Method Using Feature Pyramid Networks with Physical Constraints. *Computer Modeling in Engineering & Sciences*, 128(3):823–848, 2021. ISSN 1526-1506. doi: 10.32604/cmes.2021.016737. URL <https://www.techscience.com/CMES/v128n3/44011>.
- [10] Baotong Li, Congjia Huang, Xin Li, Shuai Zheng, and Jun Hong. Non-iterative structural topology optimization using deep learning. *Computer-Aided Design*, 115:172–180, October 2019. ISSN 0010-4485. doi: 10.1016/j.cad.2019.05.038. URL <https://www.sciencedirect.com/science/article/pii/S001044851930185X>.
- [11] Yonggyun Yu, Taeil Hur, Jaeho Jung, and In Gwun Jang. Deep learning for determining a near-optimal topological design without any iteration. *Structural and Multidisciplinary Optimization*, 59(3):787–799, March 2019. ISSN 1615-1488. doi: 10.1007/s00158-018-2101-5. URL <https://doi.org/10.1007/s00158-018-2101-5>.
- [12] Mohammad Mahdi Behzadi and Horea T. Ilies. GANTL: Towards Practical and Real-Time Topology Optimization with Conditional GANs and Transfer Learning. *Journal of Mechanical Design*, pages 1–32, October 2021. ISSN 1050-0472, 1528-9001. doi: 10.1115/1.4052757. URL <https://asmedigitalcollection.asme.org/mechanicaldesign/article/doi/10.1115/1.4052757/1121902/GANTL-Towards-Practical-and-Real-Time-Topology>.
- [13] Sumudu Herath and Udith Haputhanthri. Topologically optimal design and failure prediction using conditional generative adversarial networks. *International Journal for Numerical Methods in Engineering*, 122(23):6867–6887, December 2021. ISSN 0029-5981, 1097-0207. doi: 10.1002/nme.6814. URL <https://onlinelibrary.wiley.com/doi/10.1002/nme.6814>.
- [14] Shuai Zheng, Haojie Fan, Ziyu Zhang, Zhiqiang Tian, and Kang Jia. Accurate and real-time structural topology prediction driven by deep learning under moving morphable component-based framework. *Applied Mathematical Modelling*, 97:522–535, September 2021. ISSN 0307-904X. doi: 10.1016/j.apm.2021.04.009. URL <https://www.sciencedirect.com/science/article/pii/S0307904X21002092>.
- [15] Van-Nam Hoang, Ngoc-Linh Nguyen, Dat Q. Tran, Quang-Viet Vu, and H. Nguyen-Xuan. Data-driven geometry-based topology optimization. *Structural and Multidisciplinary Optimization*, 65(2):69, January 2022. ISSN 1615-1488. doi: 10.1007/s00158-022-03170-8. URL <https://doi.org/10.1007/s00158-022-03170-8>.
- [16] Mohammad Mahdi Behzadi and Horea T. Ilies. Real-Time Topology Optimization in 3D via Deep Transfer Learning. *Computer-Aided Design*, 135:103014, June 2021. ISSN 0010-4485. doi: 10.1016/j.cad.2021.103014. URL <https://www.sciencedirect.com/science/article/pii/S0010448521000257>.
- [17] Erva Ulu, Rusheng Zhang, and Levent Burak Kara. A data-driven investigation and estimation of optimal topologies under variable loading configurations. *Computer Methods in Biomechanics and Biomedical Engineering: Imaging & Visualization*, 4(2):61–72, March 2016. ISSN 2168-1163, 2168-1171. doi: 10.1080/21681163.2015.1030775. URL <http://www.tandfonline.com/doi/full/10.1080/21681163.2015.1030775>.
- [18] Mauricio Araya-Polo, Joseph Jennings, Amir Adler, and Taylor Dahlke. Deep-learning tomography. *The Leading Edge*, 37(1):58–66, January 2018. ISSN 1070-485X, 1938-3789. doi: 10.1190/tle37010058.1. URL <https://library.seg.org/doi/10.1190/tle37010058.1>.
- [19] Vishal Das, Ahinoam Pollack, Uri Wollner, and Tapan Mukerji. Convolutional neural network for seismic impedance inversion. *GEOPHYSICS*, 84(6):R869–R880, November 2019. ISSN 0016-8033, 1942-2156. doi: 10.1190/geo2018-0838.1. URL <https://library.seg.org/doi/10.1190/geo2018-0838.1>.
- [20] Bo Mao, Li-Guo Han, Qiang Feng, and Yu-Chen Yin. Subsurface velocity inversion from deep learning-based data assimilation. *Journal of Applied Geophysics*, 167:172–179, August 2019. ISSN 0926-9851. doi: 10.1016/j.jappgeo.2019.04.002. URL <https://www.sciencedirect.com/science/article/pii/S0926985118308905>.
- [21] Jing Rao, Fangshu Yang, Huadong Mo, Stefan Kollmannsberger, and Ernst Rank. Quantitative reconstruction of defects in multi-layered bonded composites using fully convolutional network-based ultrasonic inversion. *Journal of Sound and Vibration*, 542:117418, 2023. ISSN 0022-460X. doi: 10.1016/j.jsv.2022.117418.
- [22] Xiaoxiao Guo, Wei Li, and Francesco Iorio. Convolutional Neural Networks for Steady Flow Approximation. In *Proceedings of the 22nd ACM SIGKDD International Conference on Knowledge Discovery and Data Mining, KDD '16*, pages 481–490, New York, NY, USA, August 2016. Association for Computing Machinery. ISBN 978-1-4503-4232-2. doi: 10.1145/2939672.2939738. URL <https://doi.org/10.1145/2939672.2939738>.
- [23] Nils Thuerey, Konstantin Weissenow, Lukas Prantl, and Xiangyu Hu. Deep Learning Methods for Reynolds-Averaged Navier–Stokes Simulations of Airfoil Flows. *AIAA Journal*, 58(1):25–36, January 2020. ISSN 0001-1452, 1533-385X. doi: 10.2514/1.J058291. URL <https://arc.aiaa.org/doi/10.2514/1.J058291>.
- [24] Li-Wei Chen and Nils Thuerey. Towards high-accuracy deep learning inference of compressible flows over aerofoils. *Computers & Fluids*, 250:105707, January 2023. ISSN 0045-7930. doi: 10.1016/j.compfluid.2022.105707. URL <https://www.sciencedirect.com/science/article/pii/S0045793022003000>.
- [25] Aditya Khadilkar, Jun Wang, and Rahul Rai. Deep learning-based stress prediction for bottom-up SLA 3D printing process. *The International Journal of Advanced Manufacturing Technology*, 102(5):2555–2569, June 2019. ISSN 1433-3015. doi: 10.1007/s00170-019-03363-4. URL <https://doi.org/10.1007/s00170-019-03363-4>.
- [26] Zhenguo Nie, Haoliang Jiang, and Levent Burak Kara. Stress Field Prediction in Cantilevered Structures Using Convolutional Neural Networks. *Journal of Computing and Information Science in Engineering*, 20(1):011002, February 2020. ISSN 1530-9827, 1944-7078. doi: 10.1115/1.4044097. URL <https://asmedigitalcollection.asme.org/computingengineering/article/doi/10.1115/1.4044097/955168/Stress-Field-Prediction-in-Cantilevered-Structures>.
- [27] Xianqi Chen, Xiaoyu Zhao, Zhiqiang Gong, Jun Zhang, Weien Zhou, Xiaoqian Chen, and Wen Yao. A deep

- neural network surrogate modeling benchmark for temperature field prediction of heat source layout. *Science China Physics, Mechanics & Astronomy*, 64(11):1, September 2021. ISSN 1869-1927. doi: 10.1007/s11433-021-1755-6. URL <https://doi.org/10.1007/s11433-021-1755-6>.
- [28] Lu Lu, Pengzhan Jin, Guofei Pang, Zhongqiang Zhang, and George Em Karniadakis. Learning nonlinear operators via DeepONet based on the universal approximation theorem of operators. *Nature Machine Intelligence*, 3(3):218–229, March 2021. ISSN 2522-5839. doi: 10.1038/s42256-021-00302-5. URL <https://www.nature.com/articles/s42256-021-00302-5>.
- [29] Zongyi Li, Nikola Kovachki, Kamyar Azizzadenesheli, Burigede Liu, Kaushik Bhattacharya, Andrew Stuart, and Anima Anandkumar. Fourier Neural Operator for Parametric Partial Differential Equations, May 2021. URL <http://arxiv.org/abs/2010.08895>. arXiv:2010.08895 [cs, math].
- [30] Lu Lu, Xuhui Meng, Shengze Cai, Zhiping Mao, Somdatta Goswami, Zhongqiang Zhang, and George Em Karniadakis. A comprehensive and fair comparison of two neural operators (with practical extensions) based on FAIR data. *Computer Methods in Applied Mechanics and Engineering*, 393:114778, April 2022. ISSN 0045-7825. doi: 10.1016/j.cma.2022.114778. URL <https://www.sciencedirect.com/science/article/pii/S0045782522001207>.
- [31] Jan-Hendrik Bastek and Dennis M. Kochmann. Inverse design of nonlinear mechanical metamaterials via video denoising diffusion models. *Nature Machine Intelligence*, 5(12):1466–1475, December 2023. ISSN 2522-5839. doi: 10.1038/s42256-023-00762-x. URL <https://www.nature.com/articles/s42256-023-00762-x>.
- [32] Liang Liang, Minliang Liu, Caitlin Martin, and Wei Sun. A deep learning approach to estimate stress distribution: a fast and accurate surrogate of finite-element analysis. *Journal of The Royal Society Interface*, 15(138):20170844, January 2018. ISSN 1742-5689, 1742-5662. doi: 10.1098/rsif.2017.0844. URL <https://royalsocietypublishing.org/doi/10.1098/rsif.2017.0844>.
- [33] E. Muravleva, I. Oseledets, and D. Koroteev. Application of machine learning to viscoplastic flow modeling. *Physics of Fluids*, 30(10):103102, October 2018. ISSN 1070-6631, 1089-7666. doi: 10.1063/1.5058127. URL <https://pubs.aip.org/pof/article/30/10/103102/989209/Application-of-machine-learning-to-viscoplastic>.
- [34] Liang Liang, Minliang Liu, Caitlin Martin, and Wei Sun. A machine learning approach as a surrogate of finite element analysis-based inverse method to estimate the zero-pressure geometry of human thoracic aorta. *International Journal for Numerical Methods in Biomedical Engineering*, 34(8):e3103, August 2018. ISSN 2040-7939, 2040-7947. doi: 10.1002/cnm.3103. URL <https://onlinelibrary.wiley.com/doi/10.1002/cnm.3103>.
- [35] Ali Madani, Ahmed Bakhaty, Jiwon Kim, Yara Mubarak, and Mohammad R. K. Mofrad. Bridging Finite Element and Machine Learning Modeling: Stress Prediction of Arterial Walls in Atherosclerosis. *Journal of Biomechanical Engineering*, 141(8):084502, August 2019. ISSN 0148-0731, 1528-8951. doi: 10.1115/1.4043290. URL <https://asmedigitalcollection.asme.org/biomechanical/article/doi/10.1115/1.4043290/727399/Bridging-Finite-Element-and-Machine-Learning>.
- [36] Kaushik Bhattacharya, Bamdad Hosseini, Nikola B. Kovachki, and Andrew M. Stuart. Model Reduction And Neural Networks For Parametric PDEs. *The SMAI Journal of computational mathematics*, 7:121–157, 2021. ISSN 2426-8399. doi: 10.5802/smai-jcm.74. URL <https://smai-jcm.centre-mersenne.org/articles/10.5802/smai-jcm.74/>.
- [37] Khouloud Derouiche, Sevan Garois, Victor Champaney, Monzer Daoud, Khalil Traidi, and Francisco Chinesta. Data-Driven Modeling for Multiphysics Parametrized Problems-Application to Induction Hardening Process. *Metals*, 11(5):738, May 2021. ISSN 2075-4701. doi: 10.3390/met11050738. URL <https://www.mdpi.com/2075-4701/11/5/738>.
- [38] Moritz Flaschel, Siddhant Kumar, and Laura De Lorenzis. Unsupervised discovery of interpretable hyperelastic constitutive laws. *Computer Methods in Applied Mechanics and Engineering*, 381:113852, August 2021. ISSN 0045-7825. doi: 10.1016/j.cma.2021.113852. URL <https://www.sciencedirect.com/science/article/pii/S0045782521001894>.
- [39] Dominik K. Klein, Mauricio Fernández, Robert J. Martin, Patrizio Neff, and Oliver Weeger. Polyconvex anisotropic hyperelasticity with neural networks. *Journal of the Mechanics and Physics of Solids*, 159:104703, February 2022. ISSN 0022-5096. doi: 10.1016/j.jmps.2021.104703. URL <https://www.sciencedirect.com/science/article/pii/S0022509621003215>.
- [40] Kevin Linka, Sarah R. St. Pierre, and Ellen Kuhl. Automated model discovery for human brain using Constitutive Artificial Neural Networks. *Acta Biomaterialia*, 160:134–151, April 2023. ISSN 1742-7061. doi: 10.1016/j.actbio.2023.01.055. URL <https://www.sciencedirect.com/science/article/pii/S1742706123000661>.
- [41] Lennart Linden, Dominik K. Klein, Karl A. Kalina, Jörg Brummund, Oliver Weeger, and Markus Kästner. Neural networks meet hyperelasticity: A guide to enforcing physics. *Journal of the Mechanics and Physics of Solids*, 179:105363, October 2023. ISSN 0022-5096. doi: 10.1016/j.jmps.2023.105363. URL <https://www.sciencedirect.com/science/article/pii/S0022509623001679>.
- [42] Antoine Benady, Emmanuel Baranger, and Ludovic Chamoin. NN-mCRE: A modified constitutive relation error framework for unsupervised learning of nonlinear state laws with physics-augmented neural networks. *International Journal for Numerical Methods in Engineering*, 125(8):e7439, April 2024. ISSN 0029-5981, 1097-0207. doi: 10.1002/nme.7439. URL <https://onlinelibrary.wiley.com/doi/10.1002/nme.7439>.
- [43] Antoine Benady, Emmanuel Baranger, and Ludovic Chamoin. Unsupervised learning of history-dependent constitutive material laws with thermodynamically-consistent neural networks in the modified Constitutive Relation Error framework. *Computer Methods in Applied Mechanics and Engineering*, 425:116967, May 2024. ISSN 0045-7825. doi: 10.1016/j.cma.2024.116967. URL <https://www.sciencedirect.com/science/article/pii/S0045782524002238>.
- [44] Johannes Dornheim, Lukas Morand, Hemanth Janarthanam Nallani, and Dirk Helm. Neural Networks for Constitutive Modeling: From Universal Function Approximators to Advanced Models and the Integration of Physics. *Archives of Computational Methods in Engineering*, 31(2):1097–1127, March 2024. ISSN 1886-1784. doi: 10.1007/s11831-023-10009-y. URL <https://doi.org/10.1007/s11831-023-10009-y>.
- [45] Kailai Xu and Eric Darve. The Neural Network Approach to Inverse Problems in Differential Equations,

- January 2019. URL <http://arxiv.org/abs/1901.07758>. arXiv:1901.07758 [math].
- [46] Jens Berg and Kaj Nyström. Neural networks as smooth priors for inverse problems for PDEs. *Journal of Computational Mathematics and Data Science*, 1:100008, September 2021. ISSN 27724158. doi: 10.1016/j.jcmts.2021.100008. URL <https://linkinghub.elsevier.com/retrieve/pii/S2772415821000043>.
 - [47] Qinglong He and Yanfei Wang. Reparameterized full-waveform inversion using deep neural networks. *GEO-PHYSICS*, 86(1):V1–V13, January 2021. ISSN 0016-8033, 1942-2156. doi: 10.1190/geo2019-0382.1. URL <https://library.seg.org/doi/10.1190/geo2019-0382.1>.
 - [48] Weiqiang Zhu, Kailai Xu, Eric Darve, Biondo Biondi, and Gregory C. Beroza. Integrating deep neural networks with full-waveform inversion: Reparameterization, regularization, and uncertainty quantification. *GEO-PHYSICS*, 87(1):R93–R109, January 2022. ISSN 0016-8033, 1942-2156. doi: 10.1190/geo2020-0933.1. URL <https://library.seg.org/doi/10.1190/geo2020-0933.1>.
 - [49] Leon Herrmann, Tim Burchner, Felix Dietrich, and Stefan Kollmannsberger. On the use of neural networks for full waveform inversion. *Computer Methods in Applied Mechanics and Engineering*, 415:116278, October 2023. ISSN 00457825. doi: 10.1016/j.cma.2023.116278. URL <https://linkinghub.elsevier.com/retrieve/pii/S0045782523004024>.
 - [50] Peng Jiang, Qingyang Wang, Yuxiao Ren, Senlin Yang, and Ningbo Li. Full waveform inversion based on inversion network reparameterized velocity. *Geophysical Prospecting*, 72(1):52–67, January 2024. ISSN 0016-8025, 1365-2478. doi: 10.1111/1365-2478.13292. URL <https://onlinelibrary.wiley.com/doi/10.1111/1365-2478.13292>.
 - [51] Stephan Hoyer, Jascha Sohl-Dickstein, and Sam Greidanus. Neural reparameterization improves structural optimization, September 2019. URL <http://arxiv.org/abs/1909.04240>. arXiv:1909.04240 [cs, stat].
 - [52] Hao Deng and Albert C. To. Topology optimization based on deep representation learning (DRL) for compliance and stress-constrained design. *Computational Mechanics*, 66(2):449–469, August 2020. ISSN 1432-0924. doi: 10.1007/s00466-020-01859-5. URL <https://doi.org/10.1007/s00466-020-01859-5>.
 - [53] Liang Chen and Mo-How Herman Shen. A New Topology Optimization Approach by Physics-Informed Deep Learning Process. *Advances in Science, Technology and Engineering Systems Journal*, 6(4):233–240, July 2021. ISSN 24156698, 24156698. doi: 10.25046/aj060427. URL <https://astesj.com/v06/i04/p27/>.
 - [54] Aaditya Chandrasekhar and Krishnan Suresh. TOuNN: Topology Optimization using Neural Networks. *Structural and Multidisciplinary Optimization*, 63(3):1135–1149, March 2021. ISSN 1615-147X, 1615-1488. doi: 10.1007/s00158-020-02748-4. URL <http://link.springer.com/10.1007/s00158-020-02748-4>.
 - [55] Aaditya Chandrasekhar and Krishnan Suresh. Multi-Material Topology Optimization Using Neural Networks. *Computer-Aided Design*, 136:103017, July 2021. ISSN 0010-4485. doi: 10.1016/j.cad.2021.103017. URL <https://www.sciencedirect.com/science/article/pii/S0010448521000282>.
 - [56] Aaditya Chandrasekhar and Krishnan Suresh. Approximate Length Scale Filter in Topology Optimization using Fourier Enhanced Neural Networks. *Computer-Aided Design*, 150:103277, September 2022. ISSN 0010-4485. doi: 10.1016/j.cad.2022.103277. URL <https://www.sciencedirect.com/science/article/pii/S0010448522000574>.
 - [57] Connor N. Mallon, Aaron W. Thornton, Matthew R. Hill, and Santiago Badia. Neural Level Set Topology Optimization Using Unfitted Finite Elements, February 2024. URL <http://arxiv.org/abs/2303.13672>. arXiv:2303.13672 [cs].
 - [58] Ana P O Muller, Jessé C Costa, Clecio R Bom, Matheus Klatt, Elisangela L Faria, Marcelo P de Albuquerque, and Marcio P de Albuquerque. Deep pre-trained FWI: where supervised learning meets the physics-informed neural networks. *Geophysical Journal International*, 235(1):119–134, May 2023. ISSN 0956-540X, 1365-246X. doi: 10.1093/gji/ggad215. URL <https://academic.oup.com/gji/article/235/1/119/7176057>.
 - [59] Stefan Kollmannsberger, Divya Singh, and Leon Herrmann. Transfer Learning Enhanced Full Waveform Inversion*. In *2023 IEEE/ASME International Conference on Advanced Intelligent Mechatronics (AIM)*, pages 866–871, June 2023. doi: 10.1109/AIM46323.2023.10196158. URL <https://ieeexplore.ieee.org/document/10196158/>. ISSN: 2159-6255.
 - [60] Divya Shyam Singh, Leon Herrmann, Qing Sun, Tim Burchner, Felix Dietrich, and Stefan Kollmannsberger. Accelerating full waveform inversion by transfer learning. *in review*, 2024.
 - [61] Sinno Jialin Pan and Qiang Yang. A Survey on Transfer Learning. *IEEE Transactions on Knowledge and Data Engineering*, 22(10):1345–1359, October 2010. ISSN 1558-2191. doi: 10.1109/TKDE.2009.191. URL <https://ieeexplore.ieee.org/document/5288526>.
 - [62] Jason Yosinski, Jeff Clune, Yoshua Bengio, and Hod Lipson. How transferable are features in deep neural networks? In *Proceedings of the 27th International Conference on Neural Information Processing Systems - Volume 2*, NIPS’14, pages 3320–3328, Cambridge, MA, USA, December 2014. MIT Press.
 - [63] Peng Yan, Ahmed Abdulkadir, Paul-Philipp Luley, Matthias Rosenthal, Gerrit A. Schatte, Benjamin F. Grewe, and Thilo Stadelmann. A Comprehensive Survey of Deep Transfer Learning for Anomaly Detection in Industrial Time Series: Methods, Applications, and Directions. *IEEE Access*, 12:3768–3789, 2024. ISSN 2169-3536. doi: 10.1109/ACCESS.2023.3349132. URL <https://ieeexplore.ieee.org/document/10379639>.
 - [64] M. P. Bendsøe. Optimal shape design as a material distribution problem. *Structural optimization*, 1(4):193–202, December 1989. ISSN 1615-1488. doi: 10.1007/BF01650949. URL <https://doi.org/10.1007/BF01650949>.
 - [65] O. Sigmund. A 99 line topology optimization code written in Matlab. *Structural and Multidisciplinary Optimization*, 21(2):120–127, April 2001. ISSN 1615-1488. doi: 10.1007/s001580050176. URL <https://doi.org/10.1007/s001580050176>.
 - [66] J.S. Jensen and O. Sigmund. Topology optimization for nano-photonics. *Laser & Photonics Reviews*, 5(2):308–321, March 2011. ISSN 1863-8880, 1863-8899. doi: 10.1002/lpor.201000014. URL <https://onlinelibrary.wiley.com/doi/10.1002/lpor.201000014>.
 - [67] Rasmus E. Christiansen and Ole Sigmund. Compact 200 line MATLAB code for inverse design in photonics by topology optimization: tutorial. *Journal of the Optical Society of America B*, 38(2):510, February 2021. ISSN 0740-3224, 1520-8540. doi: 10.1364/JOSAB.405955. URL <https://opg.optica.org/abstract.cfm?URI=josa>

b-38-2-510.

- [68] Rasmus E. Christiansen and Ole Sigmund. Inverse design in photonics by topology optimization: tutorial. *Journal of the Optical Society of America B*, 38(2):496, February 2021. ISSN 0740-3224, 1520-8540. doi: 10.1364/JOSAB.406048. URL <https://opg.optica.org/abstract.cfm?URI=josab-38-2-496>.
- [69] Eddie Wadbro and Martin Berggren. Topology optimization of an acoustic horn. *Computer Methods in Applied Mechanics and Engineering*, 196(1-3):420–436, December 2006. ISSN 00457825. doi: 10.1016/j.cma.2006.05.005. URL <https://linkinghub.elsevier.com/retrieve/pii/S0045782506001745>.
- [70] Gil Ho Yoon, Jakob Søndergaard Jensen, and Ole Sigmund. Topology optimization of acoustic-structure interaction problems using a mixed finite element formulation. *International Journal for Numerical Methods in Engineering*, 70(9):1049–1075, May 2007. ISSN 0029-5981, 1097-0207. doi: 10.1002/nme.1900. URL <https://onlinelibrary.wiley.com/doi/10.1002/nme.1900>.
- [71] Jianbin Du and Niels Olhoff. Minimization of sound radiation from vibrating bi-material structures using topology optimization. *Structural and Multidisciplinary Optimization*, 33(4-5):305–321, February 2007. ISSN 1615-147X, 1615-1488. doi: 10.1007/s00158-006-0088-9. URL <http://link.springer.com/10.1007/s00158-006-0088-9>.
- [72] Jin Woo Lee and Yoon Young Kim. Rigid body modeling issue in acoustical topology optimization. *Computer Methods in Applied Mechanics and Engineering*, 198(9-12):1017–1030, February 2009. ISSN 00457825. doi: 10.1016/j.cma.2008.11.008. URL <https://linkinghub.elsevier.com/retrieve/pii/S004578250800412X>.
- [73] Junghwan Kook, Kunmo Koo, Jaeyub Hyun, Jakob S. Jensen, and Semyung Wang. Acoustical topology optimization for Zwicker’s loudness model – Application to noise barriers. *Computer Methods in Applied Mechanics and Engineering*, 237-240:130–151, September 2012. ISSN 00457825. doi: 10.1016/j.cma.2012.05.004. URL <https://linkinghub.elsevier.com/retrieve/pii/S0045782512001521>.
- [74] Eddie Wadbro. Analysis and design of acoustic transition sections for impedance matching and mode conversion. *Structural and Multidisciplinary Optimization*, 50(3):395–408, September 2014. ISSN 1615-147X, 1615-1488. doi: 10.1007/s00158-014-1058-2. URL <http://link.springer.com/10.1007/s00158-014-1058-2>.
- [75] Maria B. Dühring, Jakob S. Jensen, and Ole Sigmund. Acoustic design by topology optimization. *Journal of Sound and Vibration*, 317(3-5):557–575, November 2008. ISSN 0022460X. doi: 10.1016/j.jsv.2008.03.042. URL <https://linkinghub.elsevier.com/retrieve/pii/S0022460X08002812>.
- [76] Finn Jacobsen and Peter Moller Juhl. *Fundamentals of general linear acoustics*. John Wiley & Sons Inc, Chichester, West Sussex, United Kingdom, 2013. ISBN 978-1-118-63617-6 978-1-118-63616-9 978-1-118-63618-3.
- [77] I. Babuska, B. A. Szabo, and I. N. Katz. The p -Version of the Finite Element Method. *SIAM Journal on Numerical Analysis*, 18(3):515–545, June 1981. ISSN 0036-1429, 1095-7170. doi: 10.1137/0718033. URL <http://epubs.siam.org/doi/10.1137/0718033>.
- [78] Alexander Düster, Ernst Rank, and Barna Szabó. The p -Version of the Finite Element and Finite Cell Methods. In Erwin Stein, René Borst, and Thomas J R Hughes, editors, *Encyclopedia of Computational Mechanics Second Edition*, pages 1–35. Wiley, 1 edition, December 2017. ISBN 978-1-119-00379-3 978-1-119-17681-7. doi: 10.1002/9781119176817.ecm2003g. URL <https://onlinelibrary.wiley.com/doi/10.1002/9781119176817.ecm2003g>.
- [79] Jamshid Parvizián, Alexander Düster, and Ernst Rank. Finite cell method. *Computational Mechanics*, 41(1): 121–133, December 2007. ISSN 1432-0924. doi: 10.1007/s00466-007-0173-y. URL <https://doi.org/10.1007/s00466-007-0173-y>.
- [80] Z. Yang, M. Ruess, S. Kollmannsberger, A. Düster, and E. Rank. An efficient integration technique for the voxel-based finite cell method. *International Journal for Numerical Methods in Engineering*, 91(5):457–471, August 2012. ISSN 0029-5981, 1097-0207. doi: 10.1002/nme.4269. URL <https://onlinelibrary.wiley.com/doi/10.1002/nme.4269>.
- [81] Diederik P. Kingma and Jimmy Ba. Adam: A Method for Stochastic Optimization. *arXiv:1412.6980 [cs]*, January 2017. URL <http://arxiv.org/abs/1412.6980>.
- [82] Jeroen P. Groen, Matthijs Langelaar, Ole Sigmund, and Martin Ruess. Higher-order multi-resolution topology optimization using the finite cell method. *International Journal for Numerical Methods in Engineering*, 110(10):903–920, June 2017. ISSN 0029-5981, 1097-0207. doi: 10.1002/nme.5432. URL <https://onlinelibrary.wiley.com/doi/10.1002/nme.5432>.
- [83] Razvan Pascanu, Tomas Mikolov, and Yoshua Bengio. On the difficulty of training Recurrent Neural Networks, February 2013. URL <http://arxiv.org/abs/1211.5063>. arXiv:1211.5063 [cs].
- [84] Jingzhao Zhang, Tianxing He, Suvrit Sra, and Ali Jadbabaie. Why gradient clipping accelerates training: A theoretical justification for adaptivity, February 2020. URL <http://arxiv.org/abs/1905.11881>. arXiv:1905.11881 [cs, math].
- [85] Rasmus E. Christiansen, Boyan S. Lazarov, Jakob S. Jensen, and Ole Sigmund. Creating geometrically robust designs for highly sensitive problems using topology optimization: Acoustic cavity design. *Structural and Multidisciplinary Optimization*, 52(4):737–754, October 2015. ISSN 1615-147X, 1615-1488. doi: 10.1007/s00158-015-1265-5. URL <http://link.springer.com/10.1007/s00158-015-1265-5>.
- [86] D. A. Tortorelli and P. Michaleris. Design sensitivity analysis: Overview and review. *Inverse Problems in Engineering*, 1(1):71–105, October 1994. ISSN 1068-2767, 1029-0281. doi: 10.1080/174159794088027573. URL <https://www.tandfonline.com/doi/full/10.1080/174159794088027573>.
- [87] O. Sigmund and J. Petersson. Numerical instabilities in topology optimization: A survey on procedures dealing with checkerboards, mesh-dependencies and local minima. *Structural optimization*, 16(1):68–75, August 1998. ISSN 1615-1488. doi: 10.1007/BF01214002. URL <https://doi.org/10.1007/BF01214002>.
- [88] Tyler E. Bruns and Daniel A. Tortorelli. Topology optimization of non-linear elastic structures and compliant mechanisms. *Computer Methods in Applied Mechanics and Engineering*, 190(26):3443–3459, March 2001. ISSN 0045-7825. doi: 10.1016/S0045-7825(00)00278-4. URL <https://www.sciencedirect.com/science/article/pii/S0045782500002784>.

- [89] Blaise Bourdin. Filters in topology optimization. *International Journal for Numerical Methods in Engineering*, 50(9):2143–2158, March 2001. ISSN 0029-5981, 1097-0207. doi: 10.1002/nme.116. URL <https://onlinelibrary.wiley.com/doi/10.1002/nme.116>.
- [90] Ole Sigmund. Morphology-based black and white filters for topology optimization. *Structural and Multidisciplinary Optimization*, 33(4):401–424, April 2007. ISSN 1615-1488. doi: 10.1007/s00158-006-0087-x. URL <https://doi.org/10.1007/s00158-006-0087-x>.
- [91] Ole Sigmund. Manufacturing tolerant topology optimization. *Acta Mechanica Sinica*, 25(2):227–239, April 2009. ISSN 1614-3116. doi: 10.1007/s10409-009-0240-z. URL <https://doi.org/10.1007/s10409-009-0240-z>.
- [92] J. K. Guest, J. H. Prévost, and T. Belytschko. Achieving minimum length scale in topology optimization using nodal design variables and projection functions. *International Journal for Numerical Methods in Engineering*, 61(2):238–254, September 2004. ISSN 0029-5981, 1097-0207. doi: 10.1002/nme.1064. URL <https://onlinelibrary.wiley.com/doi/10.1002/nme.1064>.
- [93] Fengwen Wang, Boyan Stefanov Lazarov, and Ole Sigmund. On projection methods, convergence and robust formulations in topology optimization. *Structural and Multidisciplinary Optimization*, 43(6):767–784, June 2011. ISSN 1615-147X, 1615-1488. doi: 10.1007/s00158-010-0602-y. URL <https://link.springer.com/10.1007/s00158-010-0602-y>.
- [94] Lei Li and Kapil Khandelwal. Volume preserving projection filters and continuation methods in topology optimization. *Engineering Structures*, 85:144–161, February 2015. ISSN 0141-0296. doi: 10.1016/j.engstruct.2014.10.052. URL <https://www.sciencedirect.com/science/article/pii/S0141029614006579>.
- [95] Adam Paszke, Sam Gross, Francisco Massa, Adam Lerer, James Bradbury, Gregory Chanan, Trevor Killeen, Zeming Lin, Natalia Gimelshein, Luca Antiga, Alban Desmaison, Andreas Köpf, Edward Yang, Zach DeVito, Martin Raison, Alykhan Tejani, Sasank Chilamkurthy, Benoit Steiner, Lu Fang, Junjie Bai, and Soumith Chintala. PyTorch: An Imperative Style, High-Performance Deep Learning Library, December 2019. URL <http://arxiv.org/abs/1912.01703>. arXiv:1912.01703 [cs, stat].
- [96] Atılım Günes Baydin, Barak A. Pearlmutter, Alexey Andreyevich Radul, and Jeffrey Mark Siskind. Automatic differentiation in machine learning: a survey. *The Journal of Machine Learning Research*, 18(1):5595–5637, January 2017. ISSN 1532-4435.
- [97] Jorge Nocedal. Updating Quasi-Newton Matrices with Limited Storage. *Mathematics of Computation*, 35(151):773–782, 1980. ISSN 0025-5718. doi: 10.2307/2006193. URL <https://www.jstor.org/stable/2006193>.
- [98] Martin P. Bendsøe and O. Sigmund. *Topology optimization: theory, methods, and applications*. Springer, Berlin ; New York, 2003. ISBN 978-3-540-42992-0.
- [99] Krister Svanberg. The method of moving asymptotes—a new method for structural optimization. *International Journal for Numerical Methods in Engineering*, 24(2):359–373, February 1987. ISSN 0029-5981, 1097-0207. doi: 10.1002/nme.1620240207. URL <https://onlinelibrary.wiley.com/doi/10.1002/nme.1620240207>.
- [100] Krister Svanberg. A Class of Globally Convergent Optimization Methods Based on Conservative Convex Separable Approximations. *SIAM Journal on Optimization*, 12(2):555–573, January 2002. ISSN 1052-6234, 1095-7189. doi: 10.1137/S1052623499362822. URL <http://epubs.siam.org/doi/10.1137/S1052623499362822>.
- [101] Kaiming He, Xiangyu Zhang, Shaoqing Ren, and Jian Sun. Delving Deep into Rectifiers: Surpassing Human-Level Performance on ImageNet Classification. In *2015 IEEE International Conference on Computer Vision (ICCV)*, pages 1026–1034, December 2015. doi: 10.1109/ICCV.2015.123. URL <https://ieeexplore.ieee.org/document/7410480>. ISSN: 2380-7504.
- [102] K. Simonyan and A. Zisserman. Very deep convolutional networks for large-scale image recognition. *3rd International Conference on Learning Representations (ICLR 2015)*, 2015. URL <https://ora.ox.ac.uk/objects/uuid:60713f18-a6d1-4d97-8f45-b60ad8aebbce>.
- [103] Kaiming He, Xiangyu Zhang, Shaoqing Ren, and Jian Sun. Deep Residual Learning for Image Recognition. In *2016 IEEE Conference on Computer Vision and Pattern Recognition (CVPR)*, pages 770–778, June 2016. doi: 10.1109/CVPR.2016.90. URL <https://ieeexplore.ieee.org/document/7780459>. ISSN: 1063-6919.
- [104] Alex Krizhevsky, Ilya Sutskever, and Geoffrey E Hinton. ImageNet Classification with Deep Convolutional Neural Networks. In *Advances in Neural Information Processing Systems*, volume 25. Curran Associates, Inc., 2012. URL https://papers.nips.cc/paper_files/paper/2012/hash/c399862d3b9d6b76c8436e924a68c45b-Abstract.html.
- [105] Ilya Loshchilov and Frank Hutter. SGDR: Stochastic Gradient Descent with Warm Restarts, May 2017. URL <http://arxiv.org/abs/1608.03983>. arXiv:1608.03983 [cs, math].
- [106] Suryanarayanan Manoj Sanu, Alejandro M. Aragon, and Miguel A. Bessa. Neural topology optimization: the good, the bad, and the ugly, July 2024. URL <http://arxiv.org/abs/2407.13954>. arXiv:2407.13954 [cs, math].
- [107] Mohamed Abdelhamid and Aleksander Czekanski. Revisiting non-convexity in topology optimization of compliance minimization problems. *Engineering Computations*, 39(3):893–915, January 2021. ISSN 0264-4401. doi: 10.1108/EC-01-2021-0052. URL <https://doi.org/10.1108/EC-01-2021-0052>.
- [108] Leon Herrmann, Ole Sigmund, Viola Muning Li, Christian Vogl, and Stefan Kollmannsberger. Neural Networks for Generating Better Local Optima in Topology Optimization [Software], July 2024. URL <https://zenodo.org/records/12806412>.
- [109] Olaf Ronneberger, Philipp Fischer, and Thomas Brox. U-Net: Convolutional Networks for Biomedical Image Segmentation. In Nassir Navab, Joachim Hornegger, William M. Wells, and Alejandro F. Frangi, editors, *Medical Image Computing and Computer-Assisted Intervention – MICCAI 2015*, pages 234–241, Cham, 2015. Springer International Publishing. ISBN 978-3-319-24574-4. doi: 10.1007/978-3-319-24574-4_28.